UNIVERSITY OF CALIFORNIA SAN DIEGO

Tracking Surface Deformation and Magma Storage at Okmok Volcano with InSAR and GPS

A thesis submitted in partial satisfaction of the
requirements for the degree
Master of Science

in

Earth Sciences

by

Sandra Slead

Committee in charge:

Professor David Sandwell, Chair
Professor Adrian Borsa
Professor Jeffrey Gee

2019

The thesis of Sandra Slead is approved, and it is acceptable in quality and form for publication on microfilm and electronically:

_____

_____

_____

Chair

University of California San Diego

2019

DEDICATION

To my parents.

TABLE OF CONTENTS

LIST OF FIGURES

LIST OF TABLES

ACKNOWLEDGEMENTS

I am a lucky person to have so many people to thank for their support over the last year. First, thank you to David Sandwell for advising me in a way that allowed me to think independently and creatively but still provided guidance whenever needed. David fosters a close-knit research group at Scripps and the welcoming environment made me feel comfortable asking questions without intimidation. David also aided in my professional development by enabling me to present at the AGU 2018 Fall Meeting and to the San Diego Association of Geologists. I would also like to acknowledge and thank my advising/thesis committee members Jeffrey Gee and Adrian Borsa for always making time to talk to me and for inspiring me with their passion for research. Thank you to Xiaohua Xu for tirelessly helping me with many of the problems I ran into during the completion of this thesis, as well as providing suggestions that streamlined much of the data processing. Without these suggestions (and scripts), this project would have taken much longer to complete. Thank you to the Sandwell lab and the first year IGPP cohort for providing great company and constant laughter. Thank you to Hanna Asefaw for being an amazing listener, friend, and role model. Last but not least, thank you to my family for helping me in more ways than I can possibly articulate. It is a great comfort to have such a solid support system and I am forever grateful for it.

This research was supported by the National Science Foundation grant number OAC-1834807. Additionally, this work used the Extreme Science and Engineering Discovery Environment (XSEDE), which is supported by National Science Foundation grant number ACI-1548562. The data processing was completed on XSEDE's supercomputer *Comet* (designed by the San Diego Supercomputer Center and Dell) through allocation TG-EAR170007.

ABSTRACT OF THE THESIS

Tracking Surface Deformation and Magma Storage at Okmok Volcano with InSAR and GPS

by

Sandra Slead

Master of Science in Earth Sciences

University of California San Diego, 2019

Professor David Sandwell, Chair

In active volcanic regions, ground displacement measurements can be used to detect signals of a changing magma source. This thesis presents ground displacement measurements at Okmok Volcano from both Interferometric Sythetic Aperture Radar (InSAR) and Global Positioning System (GPS) data from late 2010 through the present. Comparing the data sets illuminates complications that InSAR presents when applied to a region with high seasonal variability.

Okmok is one of the most active volcanoes in the Aleutian island arc and recently erupted explosively in 2008. The data presented show that Okmok's ground surface has inflated over

the study period, indicating recharge of its magma storage. The radial symmetry of the inflation pattern suggests that the magma source causing the inflation can be represented by a Mogi source model, so the magma chamber's best fit depth and volume change over time is solved for by implementing the Mogi model as a data inversion performed on each data set. Doing so results in an estimated magma chamber depth of 3.56 kilometers and a time series of volume change that culminates in 0.05 cubic kilometers of growth.

Chapter 1

Introduction

1.1 Motivation

Understanding the interior workings of an active volcano is a valuable tool in placing constraints on the volcano's eruptive potential. Tracking changes in this plumbing system over time is especially useful because it can offer insight into the mechanisms of the eruptions themselves. This study tracks changes in the volume of magma storage beneath Okmok Volcano, adding to an existing time series of volume change that left off in 2014 [Qu et al., 2015]. Okmok is one of the most active volcanoes in the Aleutian island arc and the ground surface inflation observed since the last eruption in 2008 provides further understanding of Okmok's recharge regime and eruptive frequency.

Movement of magma in or out of a volcanic system can be observed on the surface by geodetic methods that measure ground deformation, such as interferometric synthetic aperture radar (InSAR) and the Global Navigation Satellite System (GNSS). While monitoring a volcano from space using InSAR has advantages in spatial resolution and the convenience of being able to take measurements without ever having to visit the location of interest, it suffers from a lower temporal resolution and noise-inducing environmental factors. In the case of this study, Okmok's

seasonal ice cover and high topographic relief present a challenge for InSAR processing. The impact of these challenges on the processed data is illuminated by comparing the results to those obtained instead by GNSS data from the same time and location. Because it is infeasible to instrument every active volcano in the world with GNSS receivers as a means of calibrating the comparatively plentiful InSAR data, these sources of error must be understood in order to allow for InSAR to be used alone in monitoring volcanic processes.

1.2 Geologic Context

1.2.1 Aleutian Arc

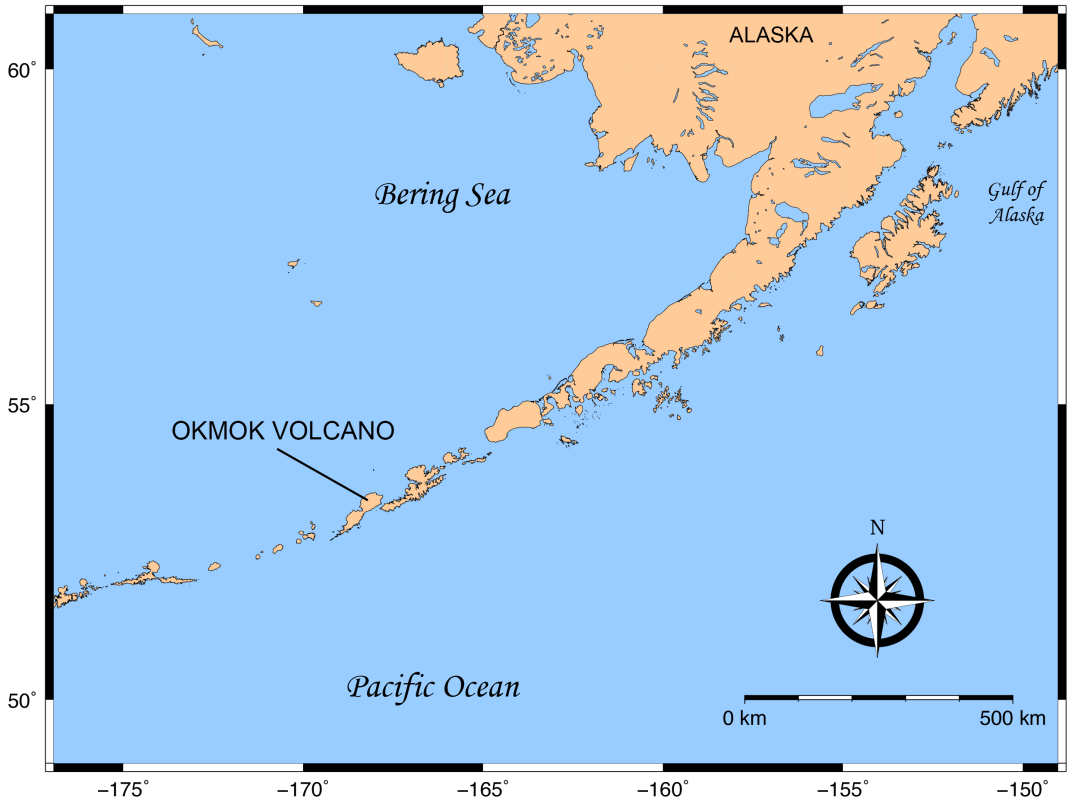

Figure 1.1: Map of the Aleutian Island Arc, highlighting Okmok Volcano's location on Umnak Island.

The study takes place in the Aleutian Arc, which is a 2,500 kilometer long chain of volcanic islands that form the northern section of the Pacific Ring of Fire. A model of arc formation by Lathram (1994) proposes that during the late Mesozoic, the Pacific plate began subducting beneath the North American plate and created a trench along the sweep of the present-day Aleutians. As oceanic lithosphere descends into the mantle at a convergent margin, it releases fluids that lower the melting point of the overlying mantle wedge, which forms magma that rises and can culminate in volcanism. As this process began on the seafloor parallel to the Aleutian trench, the newly erupted volcanic arc formed a barrier that caused sediments to pool in the Bering Sea. This positive feedback loop allowed the volcanic ridge and surface of the sedimentary basin to rise to sea level by the mid-Miocene.

Despite their apparent visual homogeneity, the volcanoes along the arc extrude a variety of lavas ranging from basalt to dacite [Fournelle et al., 1994]. Kay and Kay (1994) used patterns of seismicity and fracture zone boundaries to segment the arc into four tectonic blocks and suggest that volcanoes can be chemically described by their positions in the blocks. Volcanoes at the edges exist under an extensional stress regime which allows magma to ascend rapidly and fractionate at shallow levels, producing magmas of tholeiitic composition. In the blocks' centers where the stress regime is compressional, magmas rise more slowly and fractionate deeper, producing calc-alkaline andesites. Many other models to explain the compositional variation along the arc also exist [Kay, 1980, Marsh, 1976, Morris and Hart, 1986, Brophy and Marsh, 1986].

1.2.2 Okmok Volcano

Okmok Volcano is a basaltic shield volcano occupying the northeast section of Umnak Island at the eastern end of the Aleutian arc. Fitting in with the tectonic block model proposed by Kay and Kay (1994), Okmok is located at the margins of two rotating blocks and produces tholeiitic magmas that erupt mostly effusively to produce its relatively low shield volcano structure. It shares Umnak Island with Mount Recheshnoi and Mount Vsevidof, both of which are andesitic

stratovolcanoes with poorly known eruptive histories. Okmok, on the other hand, has been extensively studied due to its high level of activity.

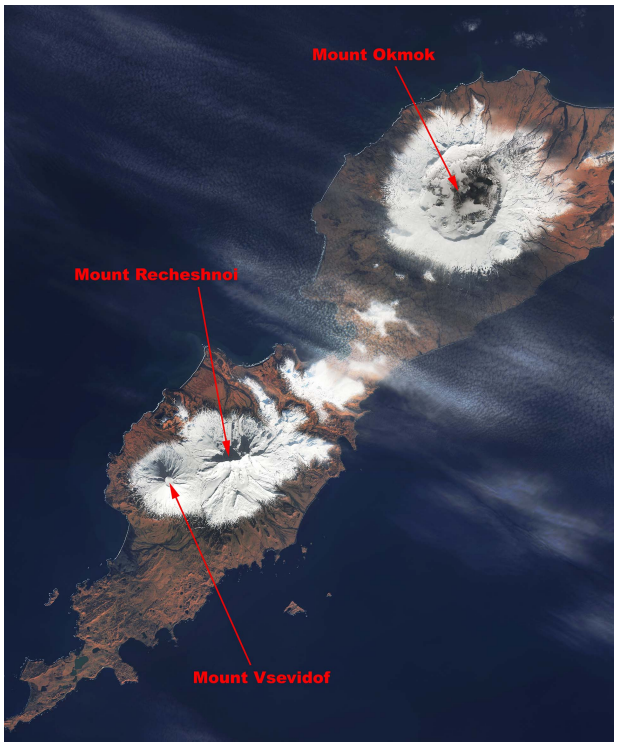

Figure 1.2: Sentinel-2A optical imagery from February 27, 2018, showing Mount Okmok and two stratovolcanoes that also occupy Umnak Island: Mount Recheshnoi and Mount Vsevidof. The data was processed using ESA's SNAP toolkit.

Two catastrophic eruptions in 12,000 and 2,050 BP erupted 30-70 km^3 of material and formed two overlapping calderas, the older of which is weakly defined by arcuate ridges outside the rim of the younger caldera [Miller et al., 1998, Finney et al., 2008]. The basin of the younger caldera is 9.5 km across and sits at an elevation of 370 meters, while the caldera rim rises to 1070 meters [Miller et al., 1998]. After the caldera-forming eruptions and since the early 1800s, Okmok is known to have erupted effusively 14 times [Miller et al., 1998, Larsen et al., 2009] but activity between these time periods is difficult to ascertain without good geologic indicators or eye-witness reports.

The two most recent 1997 and 2008 eruptions are the best-documented. The 3 month-long

eruption in 1997 was preceded by steam coming from inside the caldera [Miller et al., 1998], followed by Hawaiian/Strombolian activity, a 9 km ash plume that resulted in an air traffic advisory, and a basaltic lava flow extending 6 km [Patrick et al., 2003]. The 6 km lava flow can be seen in radar imagery as a bright area due to its higher backscatter (see Figure 1.3), and has been estimated to have a volume of 0.154 km^3 [Lu et al., 2003]. Okmok erupted again in 2008 with very little warning, as seismicity began only 5 hours prior and was barely detectable [Larsen et al., 2009]. Unlike the primarily effusive eruption of 1997, the 2008 event was highly explosive due to magma interactions with groundwater and surface water [Larsen et al., 2009].

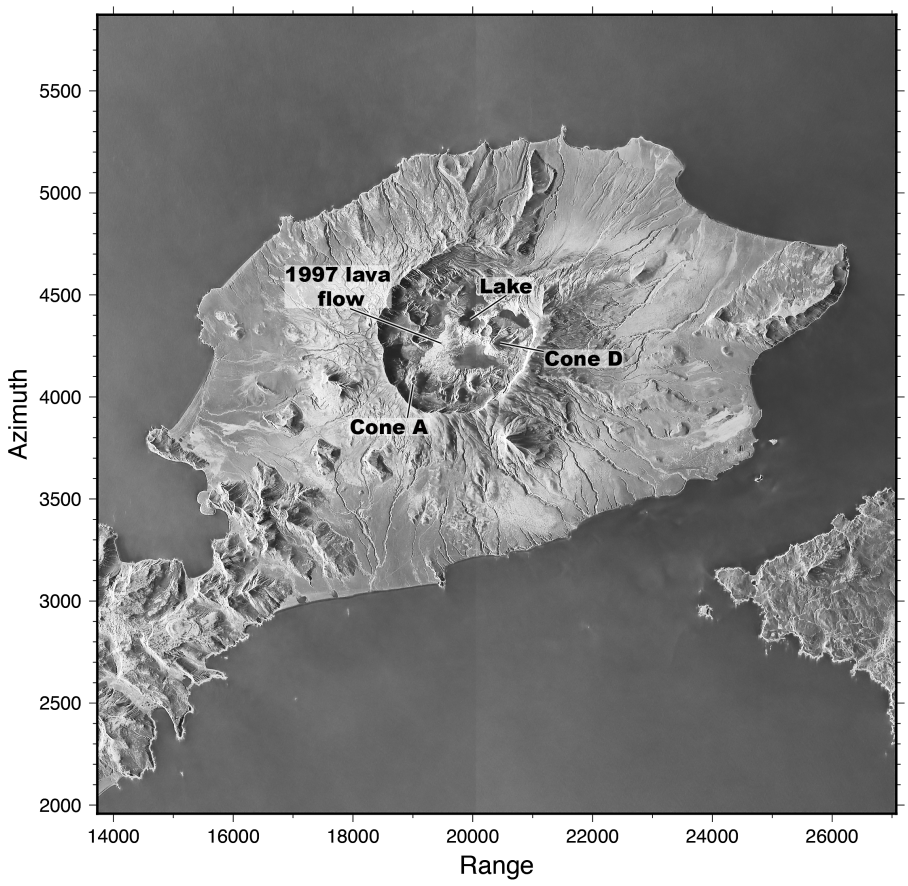

Figure 1.3: Sentinel-1 radar amplitude image of Okmok Volcano created by stacking 61 raw synthetic aperture radar images from the ascending pass, computing the average amplitude in each pixel, and performing a high pass filter and histogram equalization on the result. Image is in radar coordinates. The vertical discontinuity through the center of the image is the boundary between two subswaths of data.

1.3 Volcano Geodesy

1.3.1 Deformation

Indicators of volcanic unrest can be gas emissions, seismicity, changes in heat flow, and/or deformation of the ground surface. Deformation occurs as inflation or deflation in response to magma moving below the surface and displacing the surrounding rock. If magma intrudes the system in the form of a dike/sill injection or if a magma chamber grows as it is fed from depth, the volcano's ground surface swells. Similarly, if magma drains away or is erupted, the ground surface subsides to fill the cavity left behind. Monitoring this deformation allows for inference of these processes without actually being able to see them and can provide information about the likelihood of an eruption. Biggs et al., 2014 found that of 198 volcanoes studied, 25 both deformed and erupted, 9 erupted without any associated deformation, and the rest did not deform or erupt.

1.3.2 GPS and InSAR

Volcanic deformation is typically on the millimeter/centimeter scale, so recording it requires highly sensitive instruments. One such tool is GNSS, which is a collective term for satellite nagivation systems such as the US Global Positioning System (GPS), the Russian Global Navigation Satellite System (GLONASS), the European Union's Galileo, China's BeiDou Navigation Satellite System (BDS), and others. GPS is the most commonly used [Fernández et al., 2017] and is what is used in this thesis, so this terminology will be used from here on out instead of GNSS. GPS utilizes a constellation of 24 satellites to provide relative positions of receivers on the ground at millimeter scale accuracy. Each satellite transmits a position and time signal while receivers on the ground measure the time delay for that incoming signal (the pseudorange to the satellite) [Segall and Davis, 1997]. This time delay corresponds to position on the ground using the WGS-84 reference system, and since position is described using three coordinates,

four or more satellites are typically used simultaneously so that triangulation is more easily achieved. GPS data is usually processed to achieve daily average positions, but near-real time ($\leq$ 1 Hz) is possible and useful for events like eruptions where high temporal resolution is crucial [Fernández et al., 2017]. High temporal resolution is the greatest advantage of using GPS for geodesy, but limitations include poor spatial resolution and the necessity to visit the location of interest to install instrumentation. This is inconvenient for remote locations such as the Aleutians where field work is notoriously difficult.

InSAR provides a solution to both of these limitations but suffers from a lower temporal resolution. It offers a stable satellite remote sensing platform capable of measuring millimeter-scale ground surface displacements over an image swath tens to hundreds of kilometers wide, but repeat measurements are (in most cases) made only weeks to months apart [Lu and Dzurisin, 2014]. As the satellite flies over the sensing area, the synthetic aperture radar (SAR) antenna transmits pulses of microwave energy that scatter when they hit the ground. Some of this energy returns to the satellite and is recorded in a complex-valued SAR image as the strength of the return signal (amplitude) and the position in the wave cycle (phase). The strength of the backscattered signal depends on the terrain slope, surface roughness, and the dielectric properties of the medium. Smooth surfaces like roads and calm water result in low backscatter and appear dark in radar amplitude images, while rough surfaces like vegetation cause higher backscatter and appear bright in amplitude images [Rees, 2012]. Figure 1.3 shows an amplitude image of Okmok in which the 1997 lava flow can be seen as a bright region in the caldera while a nearby lake is seen as a dark region.

InSAR makes use of two of these complex-valued SAR images acquired over the same scene at different times by extracting the phase difference between them at each pixel:

$$\Delta\phi = \phi_1 - \phi_2 = \frac{4\pi}{\lambda}(r_1 - r_2) \tag{1.1}$$

Here, ϕ_1 and ϕ_2 are the phase values at each coregistered pixel in the two SAR images, r_1

and r_2 are the range distances from the antenna to the imaged points (see Figure1.4 for diagram), and λ is the radar wavelength [Rosen et al., 1996]. The resulting interferogram shows phase difference values wrapped between $-\pi$ and π, where each color fringe represents a contour of half a radar wavelength of propagation phase difference along the satellite's line of sight. This phase difference, however, contains other components besides just ground displacement, including curvature of the earth, topography, orbital error, ionospheric delay, tropospheric delay, and random noise. InSAR processing for the purpose of geodesy involves removing these contributions in order to isolate the desired surface deformation measurements.

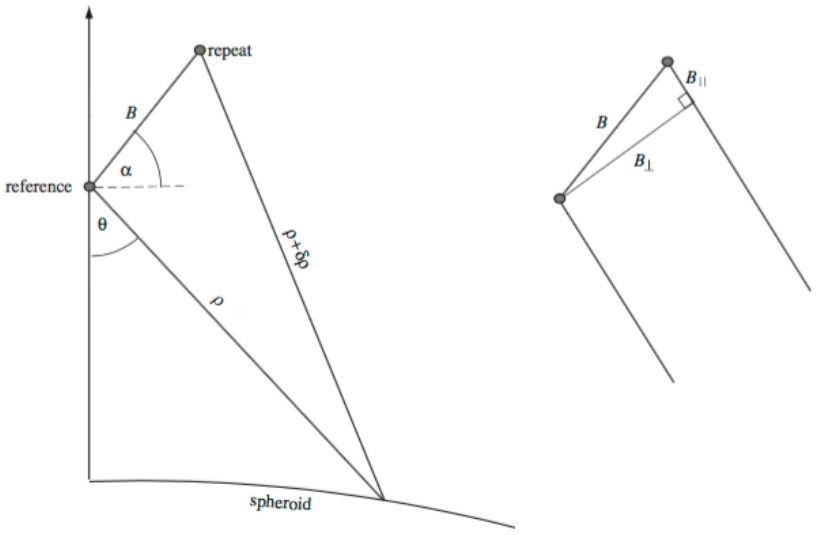

Figure 1.4: Diagram showing the geometry of repeat-pass interferometry. B is the total baseline distance between the reference and repeat tracks, ρ and $\rho + \delta\rho$ are the range from the satellite to the imaged point on the ground, θ is the satellite's look angle, and α is the angle between the baseline vector and the tangent plane. Figure from Sandwell et al., 2011.

Another complication is loss of coherence (decorrelation) due to changes in backscattering characteristics within a pixel. Equation 1.1 makes the assumption that $\Delta\phi$ represents only the difference in propagation phase, assuming that the backscatter phase difference is zero because the scattering characteristics of the pixels remain the same between images. When this assumption fails, the result is loss of coherence in those pixels. Coherence (γ) is estimated for each pixel via

cross-correlation of the image pair:

$$\gamma = \frac{|< c_1 c_2^* >|}{(< c_1 c_1^* >< c_2 c_2^* >)^{1/2}} \tag{1.2}$$

where c_1 and c_2 are the complex valued pixels of the two raw SAR images forming the interferogram and the asterisk denotes complex conjugation. This computation is done in practice by spatial averaging with a rectangular filter, so the brackets denote statistical expectation [Rosen et al., 1996]. Regions of an interferogram that fall below a threshold defined by the user are considered decorrelated and therefore useless. Decorrelation can be caused by imaging a target from look angles that are too different, volumetric backscattering effects caused by soil or snow, and/or temporal effects from other environmental changes over time. To avoid decorrelation due to imaging geometry, the distance between the satellites between repeat passes must be considered. The critical baseline is the maximum distance allowable before decorrelation will be too great (see Figure 1.4), so interferograms should not be made from scenes exceeding this baseline. Volumetric backscattering is dependent on the radar wavelength: since L band (15-30 cm) has a longer wavelength than C band (3.8 -7.5 cm), it can more easily penetrate vegetation, soil, and snow. Lastly, temporal decorrelation can be avoided by connecting SAR scenes that span short time intervals (depending on how quickly the environment is changing), or by selecting scenes that sample the same time of year so that decorrelation from seasonal changes can be minimized.

1.3.3 Modeling

A well constrained geodetic model can use ground deformation data obtained by InSAR or GPS to infer the location/depth, shape, and pressure change of a magma reservoir below the surface. While the reservoir's pressure change can give some indication of potential for an eruption, the reservoir's shape provides an idea of how the volcano is fed from depth. Some possible reser-

voir shapes are a point source [Mogi, 1958, Okada, 1992], a sphere [McTigue, 1987], an oblate spheroid [Davis, 1986], a rectangular tensile dislocation [Yang and Davis, 1986, Okada, 1992], or a horizontal circular crack [Fialko et al., 2001]. These models can be used by representing Earth's crust as a materially homogeneous and mechanically isotropic elastic half-space in which there is one planar surface bounding a region extending infinitely below it [Lisowski, 2007], but layered half-space and finite element models are also used.

Unfortunately there are many complications in building a well constrained model, due to assumptions/oversimplification of the natural system, non-unique solutions, and uncertainty in the data. As an example, the deeper the source, the more difficult it is to use surface deformation to ascertain the source's shape due to upward continuation of the deformation signal [Steketee, 1958]. Regardless of these limitations, modeling ground deformation can still provide useful insights to the plumbing system of a volcano, especially when a time series of deformation is available that provides a relative sense of activity within a time period. In an ideal situation, geodetic data is joined by other data such as seismic tomography or geochemical analysis that can place additional constraints on the model.

1.4 Previous Work on Okmok Volcano

Okmok's magma chamber dynamics before, during, and after the 1997 and 2008 eruptions have been considered in many studies using geodesy, seismic tomography, and geochemical analysis. Okmok has had SAR coverage suitable for interferometry between various satellites since 1992, so deformation since then has been recorded with variable temporal resolution. This variability is partially due to the differences in repeat cycles between satellite systems, but is also due to snow-related decorrelation of interferograms spanning winter months. Deformation associated with the 1997 eruption consisted of 12 cm of uplift centered on the caldera leading up to the event (as measured starting in 1992), coeruptive deflation of 140 cm from 1995-1997,

and posteruptive inflation of 9 cm until 1998 [Mann et al., 2002, Lu et al., 2005]. Mann et al., 2002 modeled the magma chamber driving this inflation/deflation cycle as a shallow Mogi point source at a depth ranging from 2.5 - 5.1 km. The study also suggests that since the modeled magma chamber location is horizontally offset from where the lava erupted on the caldera floor at Cone A, some lateral migration of magma may have occurred (see Figure 1.5). Another study argues that the homogeneous elastic half-space assumption of the Mogi source cannot accurately describe the rheology seen in seismic tomography data, and that there is a pressure discrepancy by an order of magnitude between that which is required by the rheology and the optimized shallow chamber depth using only InSAR/GPS data [Masterlark et al., 2010]. Masterlark et al., 2010 instead implemented a viscoelastic finite element model to account for both ambient noise tomography and geodetic data, finding a magma chamber depth of 4-6 km and a magma mass flux matching the amount of lava extruded during the 1997 eruption.

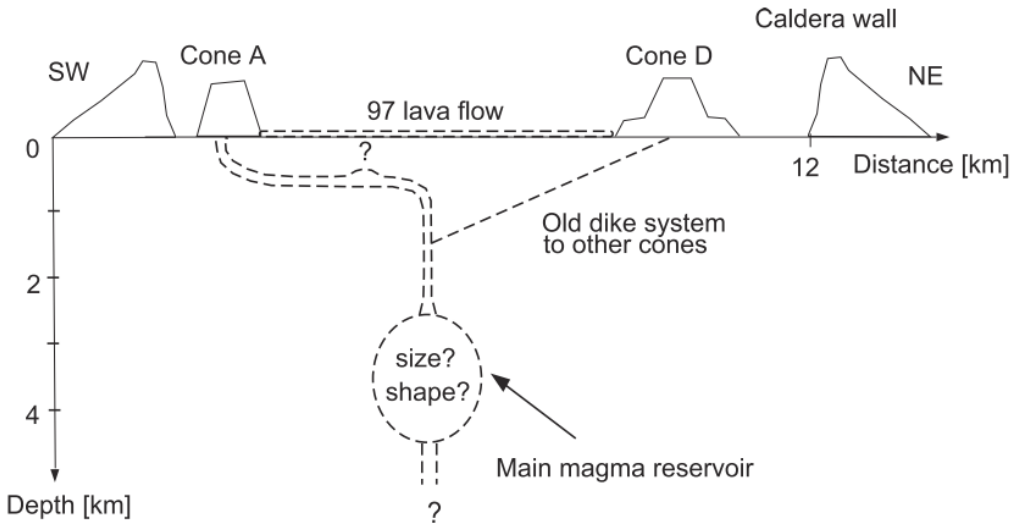

Figure 1.5: Figure from Mann et al., 2002 showing the proposed structural model of Okmok as interpreted from deformation modeling results.

The period between the 1997 and 2008 eruptions is of great interest because it offers insight to Okmok's recharge system in an absolute sense. Both InSAR [Lu et al., 2005, Lu et al., 2010,

Biggs et al., 2010] and GPS [Miyagi et al., 2004, Fournier et al., 2009, Biggs et al., 2010] demonstrate that Okmok inflated through this time period with a variable rate. These geodetic studies all suggest Mogi sources with depths in the range of 2 - 3.2 km, but again, seismic tomography suggests a more complicated source geometry. One such study used seismic data from 2003-2009 to find that there is a shallow anomaly from the surface to 2 km that could be from caldera fill, groundwater, and/or pockets of magma, and that the larger low velocity zone (LVZ) magma storage is at a depth of 4-6 km [Ohlendorf et al., 2014]. As with Masterlark et al., 2010, the interpretation by Ohlendorf et al., 2014 of the deeper LVZ as being a magma reservoir implies that the magma was in a molten state through this time period. Another study using GPS data found that the months leading up to the 2008 eruption were marked by potential lateral movement of the modeled inflation source to the southeast, closer to the eventual eruption vent [Freymueller and Kaufman, 2010]. The study states that other scenarios are also consistent with the data, which suggests that a higher spatial resolution such as that provided by InSAR could help with this ambiguity.

The 2008 eruption provided a wealth of useful data due to the presence of continuous GPS stations in addition to InSAR coverage by 5 satellites. Yet another source model was proposed by Freymueller and Kaufman (2010), in which a shallow 2.1 km source inflated immediately after the eruption as it was fed by a deeper source that concurrently deflated. Lu and Dzurisin (2010) defined a storage zone at 3 km as a sponge-like network of interconnected fractures and melt zones that pressurizes and depressurizes as it is tapped from the top down, with magma funneled to its eruptive locations via a ring fracture system around the caldera. Taking into account the phreatomagmatic nature of the eruption, Lu and Dzurisin (2010) also modeled a collapsing tabular source at 0.5 km depth and attributed it to withdrawal of groundwater that interacted with rising magma to induce the eruption. Another study used geochemical analysis of ejecta from the eruption and proposed that Okmok's magma system is a mush column containing multiple magma bodies with a common replenishment source but varying geochemical signatures

[Larsen et al., 2013]. Larsen et al., 2013 agrees with the geodetic studies in that it suggests that the 2008 eruption was triggered by an influx of melt originating from a deep 3-6 km source that intersected a more shallow 2 km source (see Figure 1.6).

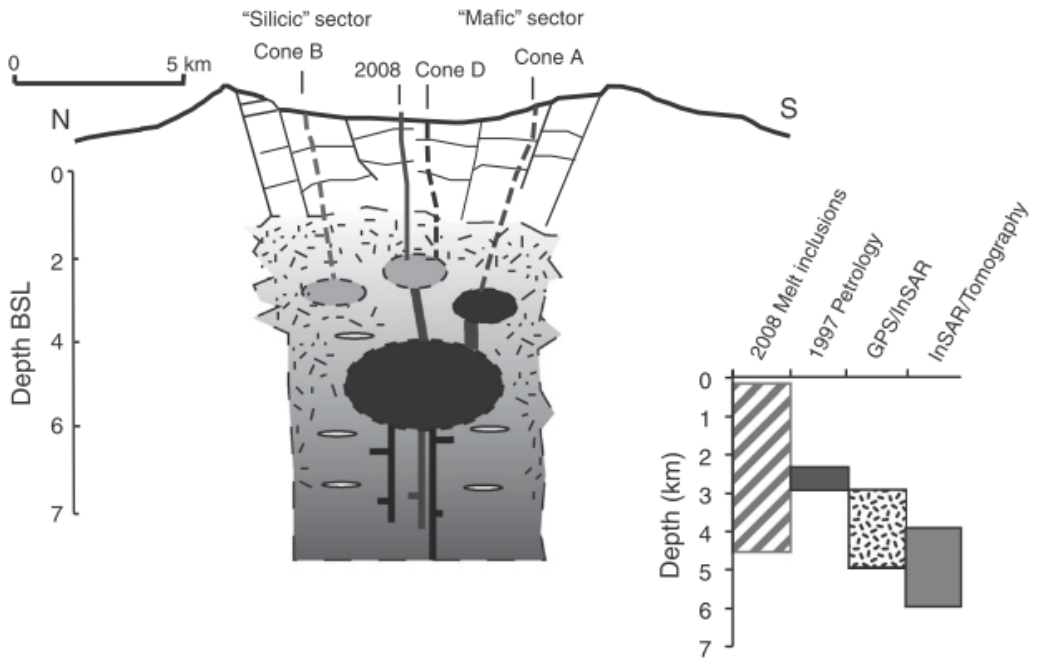

Figure 1.6: Figure from Larsen et al., 2013 showing a model of Okmok's magma plumbing system as interpreted by geochemical analysis of extruded materials.

Chapter 2

Methods and Results

This thesis utilizes both GPS and InSAR data and compares modeling results obtained by both. The GPS data will first be discussed, followed by the three InSAR data sets: ascending Sentinel-1, descending Sentinel-1, and ascending ALOS-2. Once the data and the processing methods have been introduced, the modeling approach will be presented.

2.1 GPS Data

Three continuous GPS stations (OKCE, OKFG, OKSO) were installed at Okmok Volcano in 2002 by the Alaska Volcano Observatory and the U.S. Geological Survey. They have been continuously recording data through the present. One additional station (OKNC) was added to the northern portion of the caldera in 2010 in response to the 2008 eruption. The station locations are shown in Figure 2.1 and the temporal distribution of the data is shown in Figure 2.3. The data is processed and made available for download through the Nevada Geodetic Laboratory [Blewitt, 2018]. This study uses the 24-hour final solutions version of this data processed using the North America (NA12) reference frame and the GIPSY-OASIS-II software package. Each of the four stations has a data file consisting of a time series of daily positions in the east, north, and vertical components. These time series show deformation events at Okmok since the sites

began recording, namely the pre-2008 inflation, 2008 eruption, and post-eruptive inflation since then. See Figure 2.2 for ground displacements in all three directions for each of the sites. For this study, the data was temporally smoothed by applying a median filter with a width of 7 days. Previous studies have considered the data prior to 2014 [Biggs et al., 2010, Fournier et al., 2009, Freymueller and Kaufman, 2010, Qu et al., 2015], but there has not yet been a study using the most recent 2014 - 2019 data.

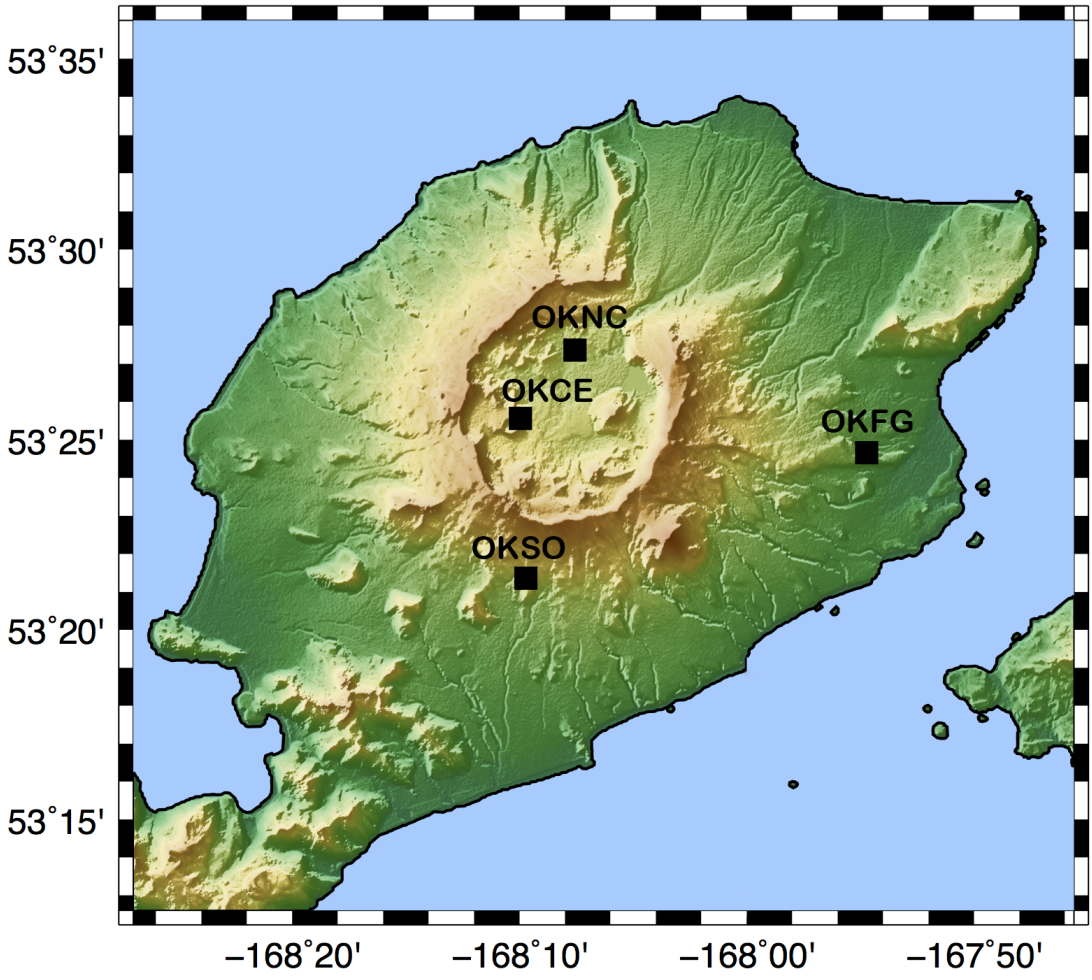

Figure 2.1: Map showing the locations of the four GPS stations on Okmok Volcano.

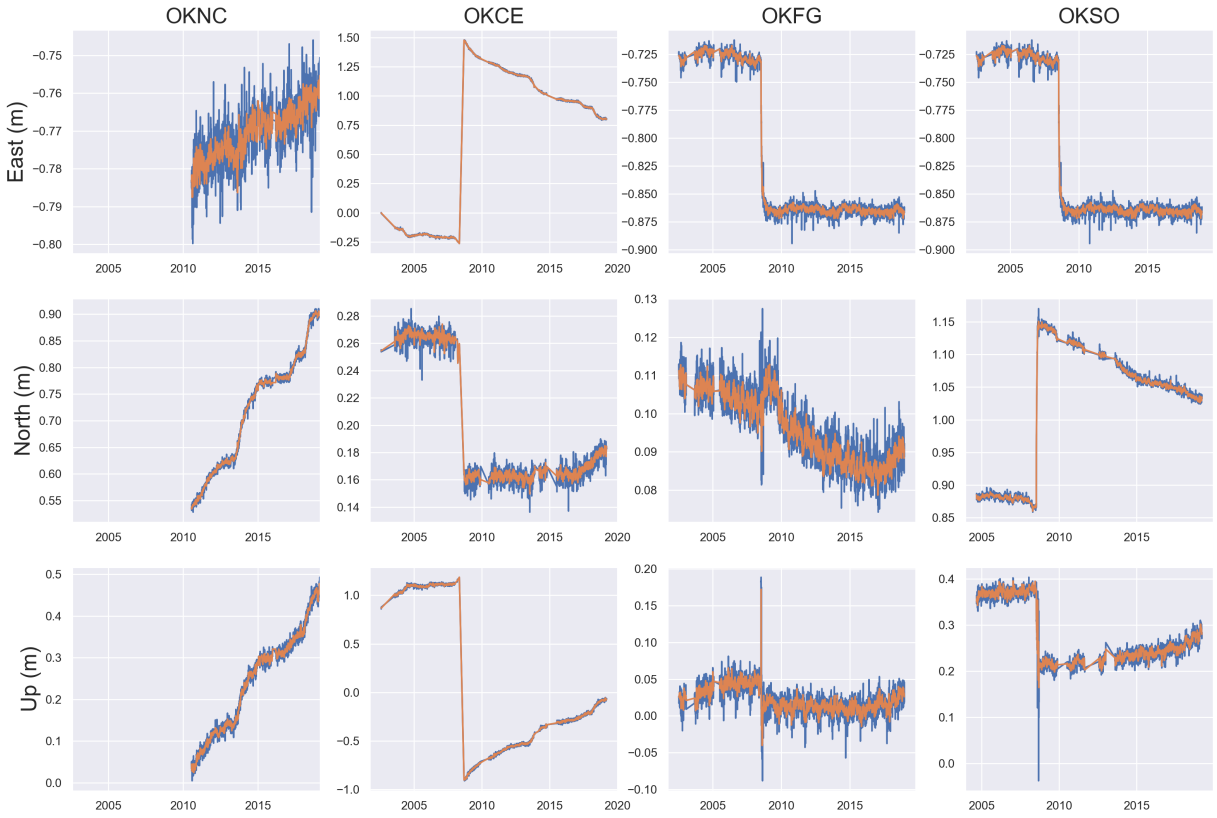

Figure 2.2: East, North, and vertical displacements in millimeters for each of the four GPS stations. Blue lines denote unfiltered data while orange lines denote data that has been filtered with a median filter set to a width of 7 days. The sharp change in 2008 seen in many of the time series marks the 2008 eruption.

2.2 InSAR Data

Three InSAR data sets were generated by processing interferograms from Sentinel-1's ascending and descending passes as well as ALOS-2's ascending pass. The temporal distribution of these data, as well as that of the GPS data, is summarized in Figure 2.3. The orbital information for these data are summarized in Table 2.1.

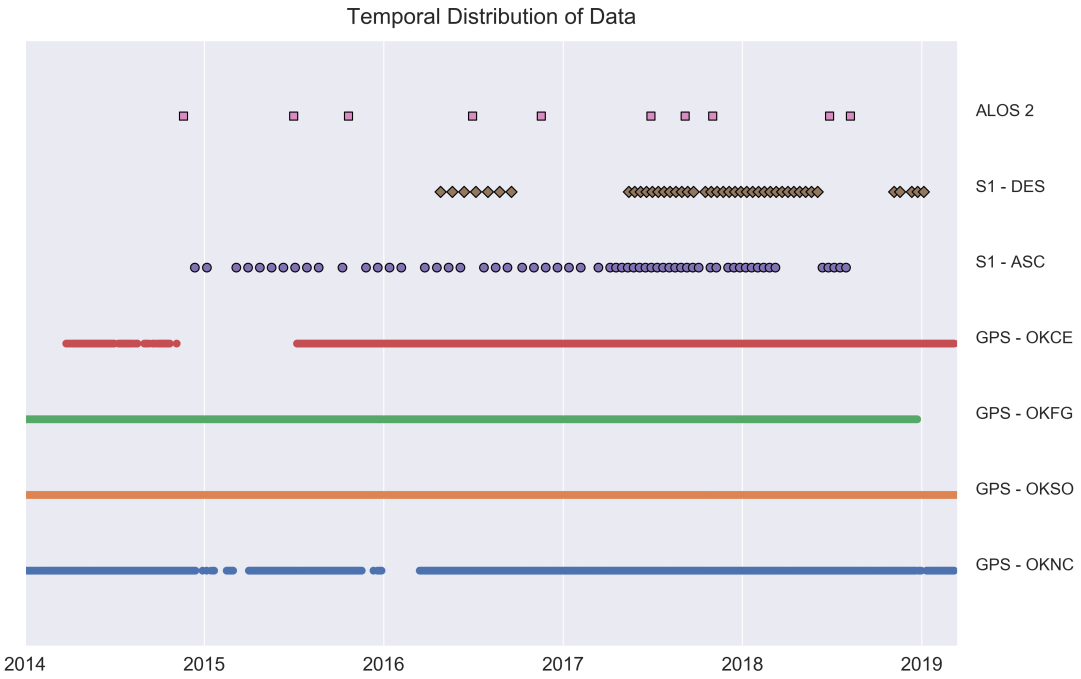

Figure 2.3: Temporal distribution of the three InSAR data sets and the four GPS stations. OKCE, OKFG, and OKSO also have data extending back to 2002, and OKNC has data extending back to 2010.

Satellite	Flight Dir.	Rel. Orbit	Frame	Mode	Scenes	Interferograms
Sentinel-1	Ascending	95	NA	TOPS	61	240
Sentinel-1	Descending	44	NA	TOPS	45	343
ALOS-2	Ascending	93	1060	STRIPMAP	10	45

Table 2.1: Summary of SAR and InSAR data information.

2.2.1 Sentinel-1

Sentinel-1 is a two-satellite constellation operated by the European Space Agency (ESA). The satellites (A and B) share an orbital plane on a sun synchronous, near-polar orbit with a 12-day repeat cycle. They are both equipped with a C-band synthetic aperture radar with a wavelength of 5.547 cm. Sentinel-1A has been providing data since 2014 and Sentinel-1B since

2016. This study takes advantage of all the data available as of December 2018 over Okmok Volcano, which is 61 scenes from the ascending pass and 45 scenes from the descending pass. While the ascending data begins in early 2015 and has relatively few gaps, the descending data begins later and is far more sparse (see Figure 2.3 for a plot of temporal data coverage).

To make the interferograms, the ascending and descending data must be treated separately due to their different viewing geometries and spatial coverage. From the 61 ascending scenes, 207 interferograms were made using the open source InSAR processing software package GMTSAR [Sandwell et al., 2011]. The basic processing workflow in GMTSAR is as follows: focus and align the stack of Single Look Complex (SLC) images from the space agency, map topography into phase, form the complex interferogram, then filter, unwrap, and geocode the interferogram. The 207 ascending Sentinel-1 interferograms were made by connecting scenes that are less than 50 days apart in time and less than 100 meters apart in baseline. An additional 33 interferograms were made by connecting yearly summer-summer scenes. This was done because use of summer scenes results in interferograms with good coherence, as opposed to interferograms created using winter scenes, which are decorrelated due to snow cover (Figure 2.5). These extra pairs help with stability during the time series construction discussed in section 2.3. All interferograms were filtered by a gaussian filter with a wavelength of 200 meters, unwrapped using the SNAPHU algorithm [Chen and Zebker, 2000], and detrended by subtracting a linear trend computed for each interferogram.

The persistent scatterers method was attempted on the ascending Sentinel-1 data in order to mitigate the winter decorrelation, and is discussed in depth in Appendix A. It was not effective because the method requires that there be isolated dependable regions within decorrelated regions. Since Okmok's snow cover completely covers the area of interest, there are no dependable scatterers such as rock outcroppings that are left uncovered.

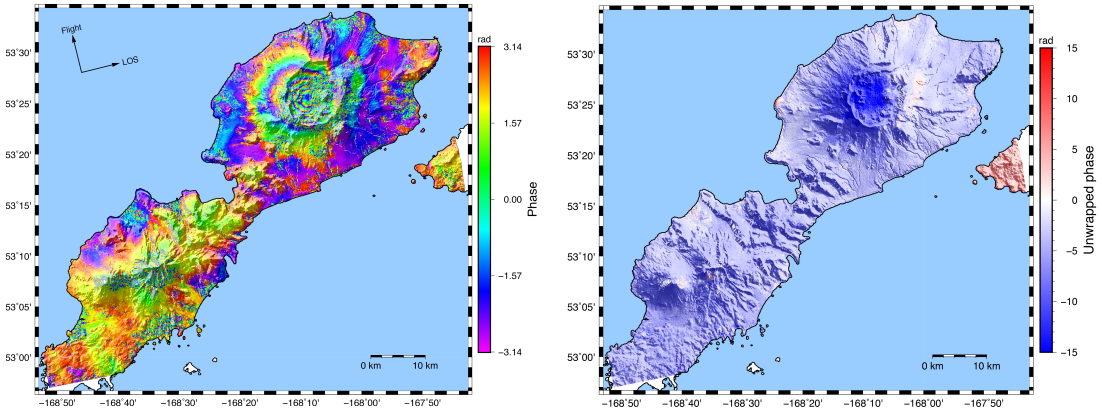

(a) Wrapped phase

(b) Unwrapped phase

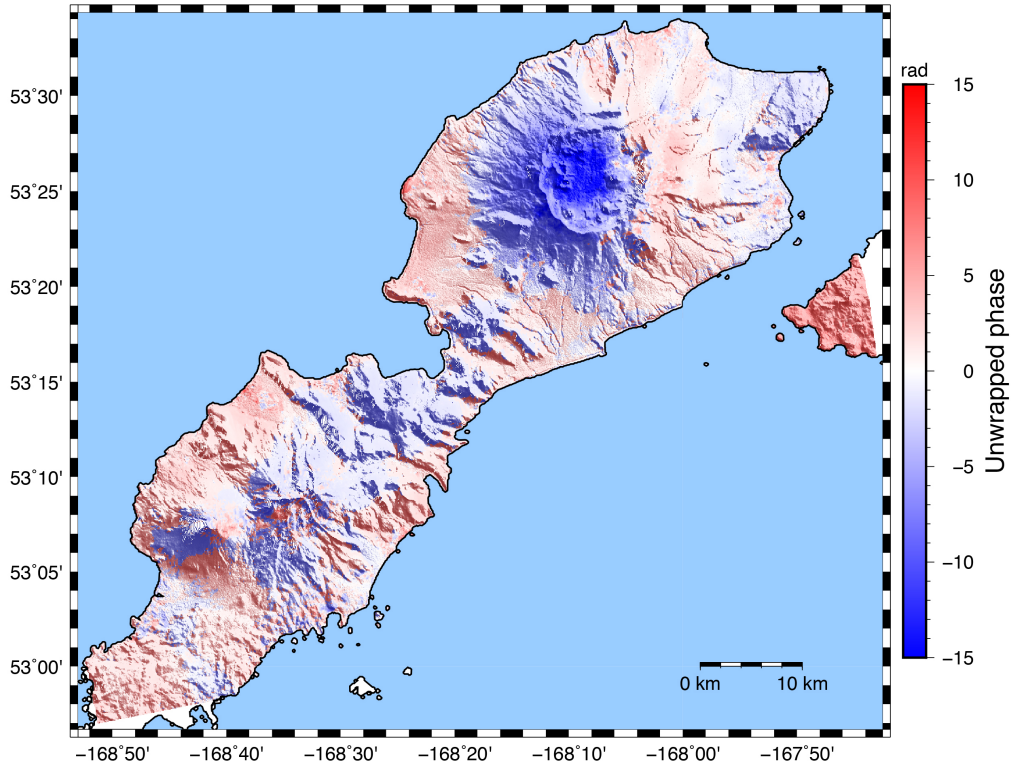

(c) Unwrapped phase, detrended

Figure 2.4: Ascending Sentinel-1 interferogram spanning June 27, 2017 - June 22, 2018. (a) shows wrapped phase, (b) shows phase after unwrapping using SNAPHU, and (c) shows unwrapped phase after being detrended by subtracting a linear trend. The leftward offset of the deformation pattern with respect to the caldera is due to the viewing geometry of the satellite as it looks down on the scene to the right. Negative phase values in the unwrapped phase correspond to decreasing range distance between the satellite and surface observational point, implying inflation of the ground surface. These maps also show shaded topography to provide regional context.

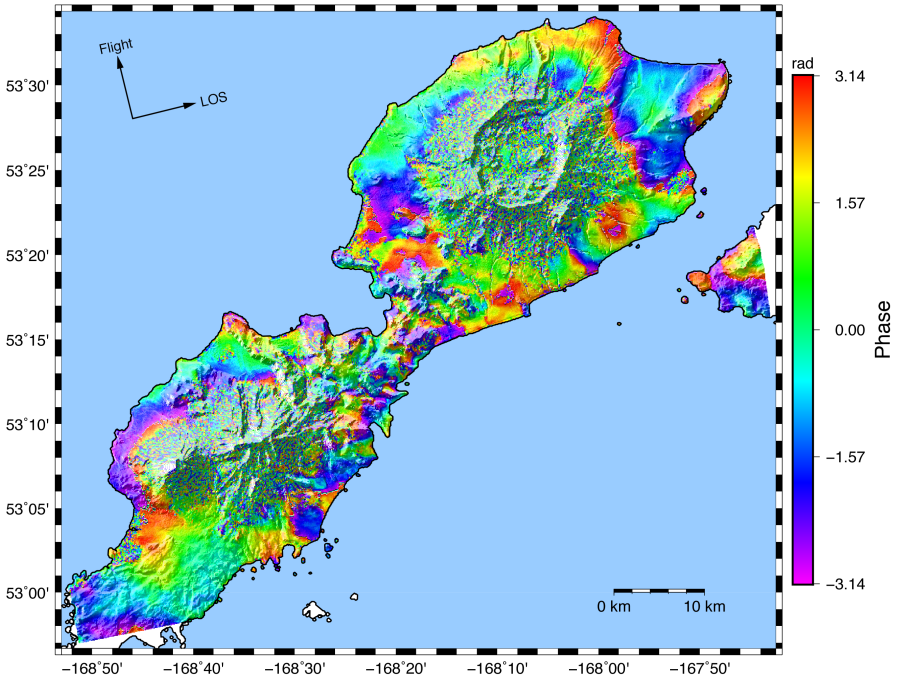

Figure 2.5: Winter pair interferogram spanning December 24, 2017 - March 6, 2018. Snow cover in the region causes decorrelation in interferograms spanning winter months, primarily in areas of high topography.

The descending Sentinel-1 data were processed similarly in that 288 interferograms were made using GMTSAR from connecting scenes with a temporal threshold of 50 days and a baseline threshold of 100 meters. 55 summer-summer pair interferograms were additionally made. All interferograms were filtered with a gaussian filter of 200 meter wavelength, unwrapped using the SNAPHU algorithm, and detrended. Like the ascending Sentinel-1 interferograms, the descending interferograms created from winter scenes are decorrelated due to snow cover. More interferograms were made for the descending Sentinel-1 data than for the ascending data because there are fewer usable scenes and therefore a greater need for added stability during the time series construction step (section 2.3).

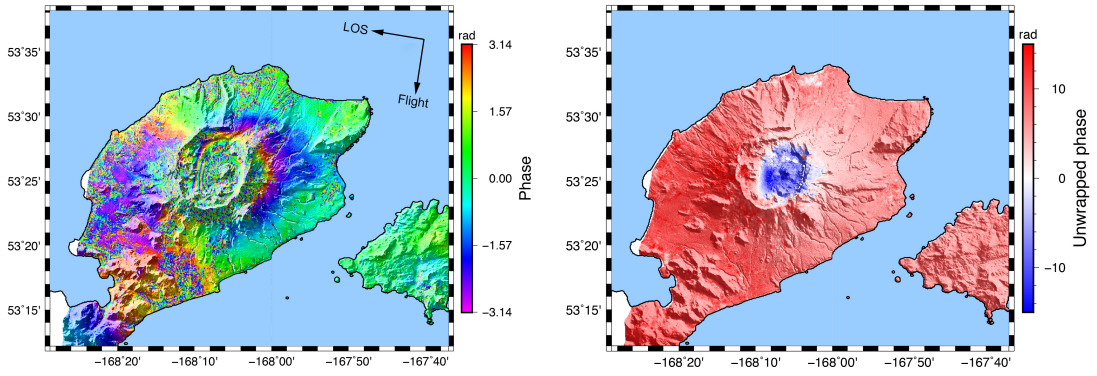

(a) Wrapped phase

(b) Unwrapped phase

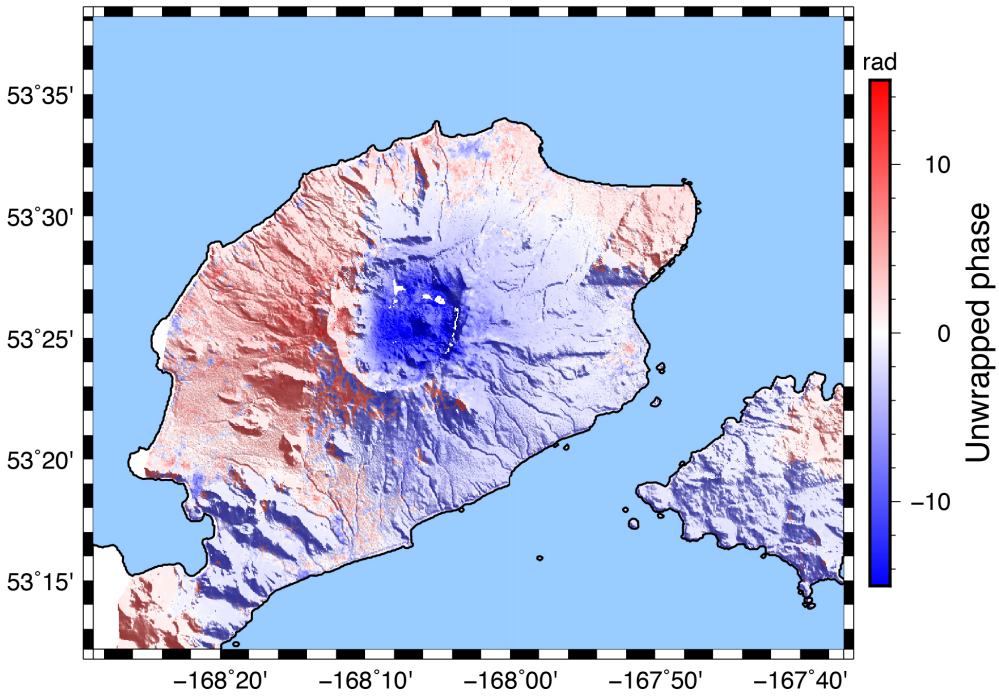

(c) Unwrapped phase, detrended

Figure 2.6: Descending Sentinel-1 interferogram spanning June 29, 2017 - May 31, 2018. Note that the timespan of this interferogram is similar to that of Figure 2.4, but the deformation pattern is now skewed to the right due to the viewing geometry of the satellite as it flies in the opposite direction. (a) shows wrapped phase, (b) shows phase after unwrapping using SNAPHU, and (c) shows unwrapped phase after being detrended by subtracting a linear trend. Negative phase values in the unwrapped phase correspond to decreasing range distance between the satellite and surface observational point, implying inflation of the ground surface. These maps also show shaded topography to provide regional context.

2.2.2 ALOS-2/PALSAR-2

The ALOS-2 satellite is operated by the Japanese Aerospace Exploration Agency (JAXA) and has an L-band synthetic aperture radar called PALSAR-2 with a 22.9 cm wavelength. Its longer wavelength compared to that of Sentinel-1 makes it less susceptible to decorrelation caused by vegetation, soil, and snow, but more sensitive to ionospheric effects. Ten ascending stripmap mode scenes from primarily summer months were obtained over Okmok Volcano spanning late 2015 through late 2018. From these, 45 interferograms were made using GMTSAR by making every possible connection between pairs, regardless of temporal or baseline threshold. These were filtered with a gaussian filter with a wavelength of 300 meters, unwrapped using SNAPHU, and detrended in the same manner as described for the Sentinel-1 interferograms.

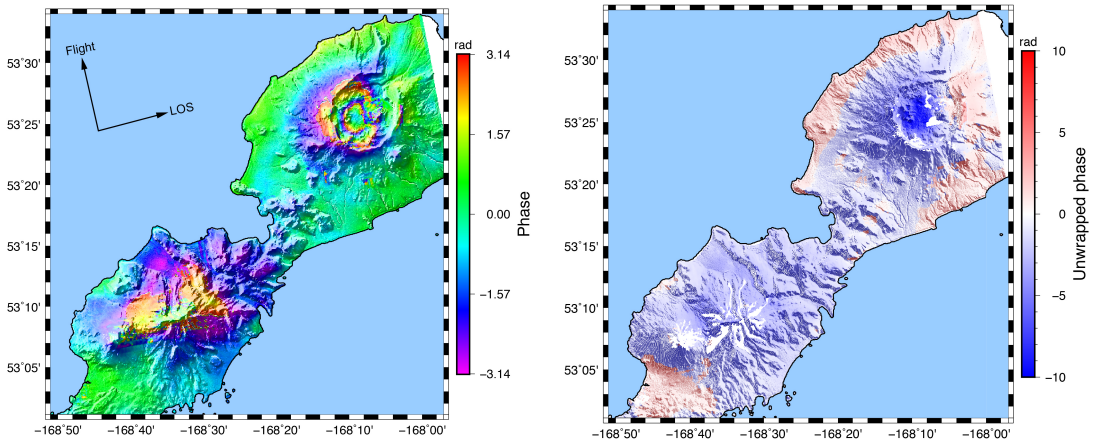

(a) Wrapped phase

(b) Unwrapped phase

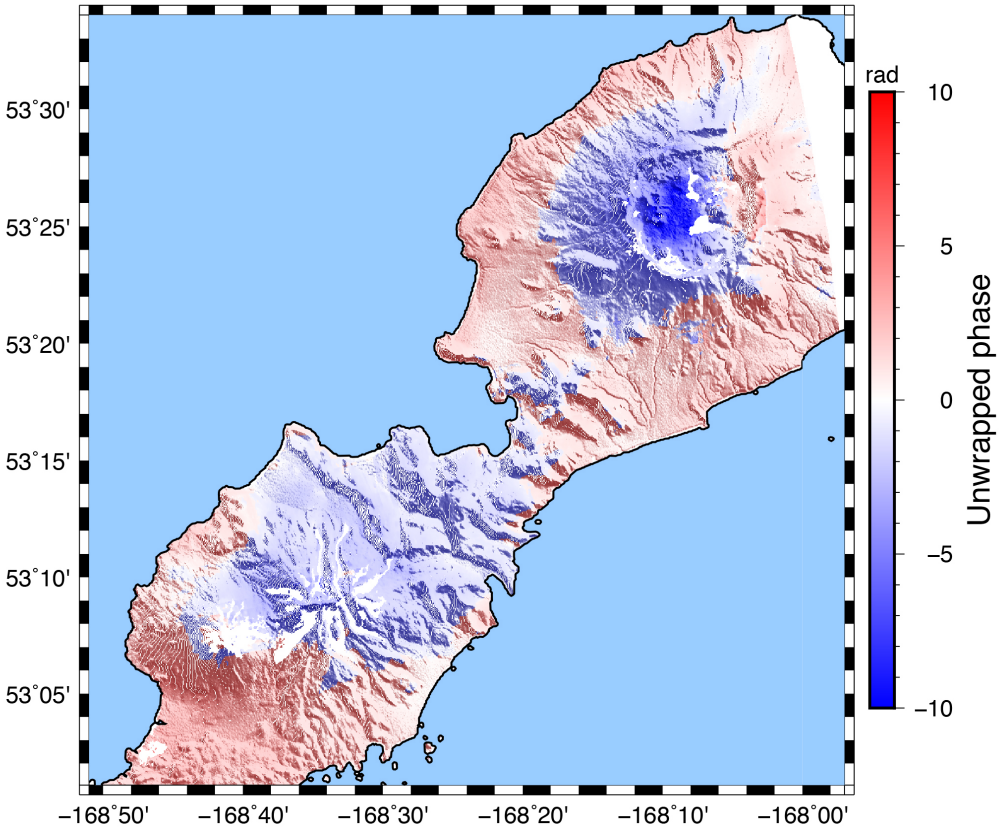

(c) Unwrapped phase, detrended

Figure 2.7: Ascending ALOS-2 interferogram spanning October 19, 2015 - August 6, 2018. Despite the interferogram spanning three years, coherence is maintained through the image due to ALOS-2's L-band radar wavelength. (a) shows wrapped phase, (b) shows phase after unwrapping using SNAPHU, and (c) shows unwrapped phase after being detrended by subtracting a linear trend. Negative phase values in the unwrapped phase correspond to decreasing range distance between the satellite and surface observational point, implying inflation of the ground surface. These images also show shaded topography to provide regional context.

2.3 Creating the Time Series: SBAS

The interferograms generated for each data set are not adjacent in time; instead, they overlap with one another and span a variety of time intervals. The last step in the InSAR data treatment is to use these interferograms to make a time series of cumulative deformation using the Small Baseline Subset (SBAS) algorithm [Berardino et al., 2002]. SBAS uses a singular value decomposition method based on a minimum-norm criterion of the deformation rate to estimate that deformation rate between each SAR scene acquisition. This estimation relies on the interferograms having small baselines and overlapping one another in time. Because snow in the winter scenes causes decorrelation, the summer-summer pairs were appended to each of three InSAR data sets to make connections that bridge the winter gaps in which the data is unreliable.

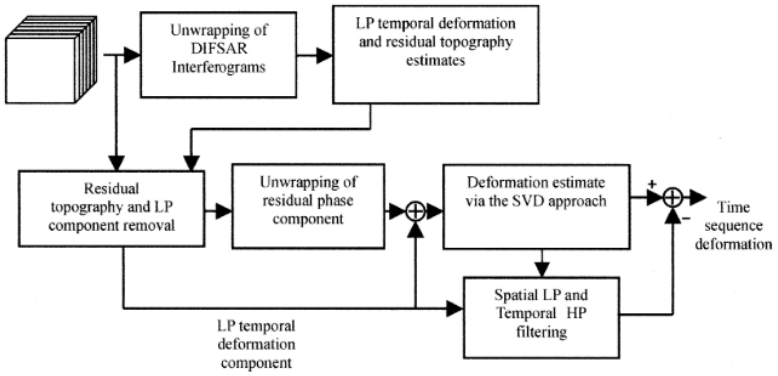

Figure 2.8: Block diagram from Bernardino et al., 2002 detailing the SBAS algorithm.

The implementation of SBAS in this study also includes correction for the atmospheric phase delay, which is important for an area of high topographic relief such as the Aleutians. This correction involves stacking interferograms that share a common scene and subtracting the estimated atmospheric contribution, leaving only tectonic signal [Tymofyeyeva and Fialko, 2015]. See the following figures for the cumulative displacements estimated by SBAS for each of the InSAR data sets.

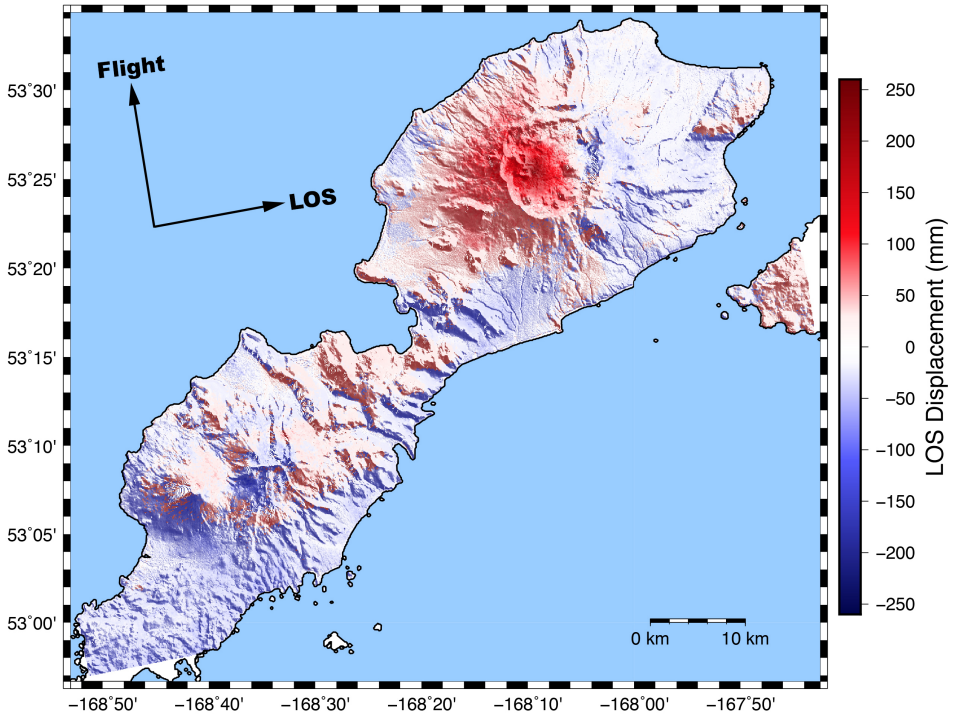

Figure 2.9: SBAS result for ascending Sentinel-1. This map shows the cumulative displacement from the first sensing date on January 3, 2015 to the last sensing date on July 28 2018.

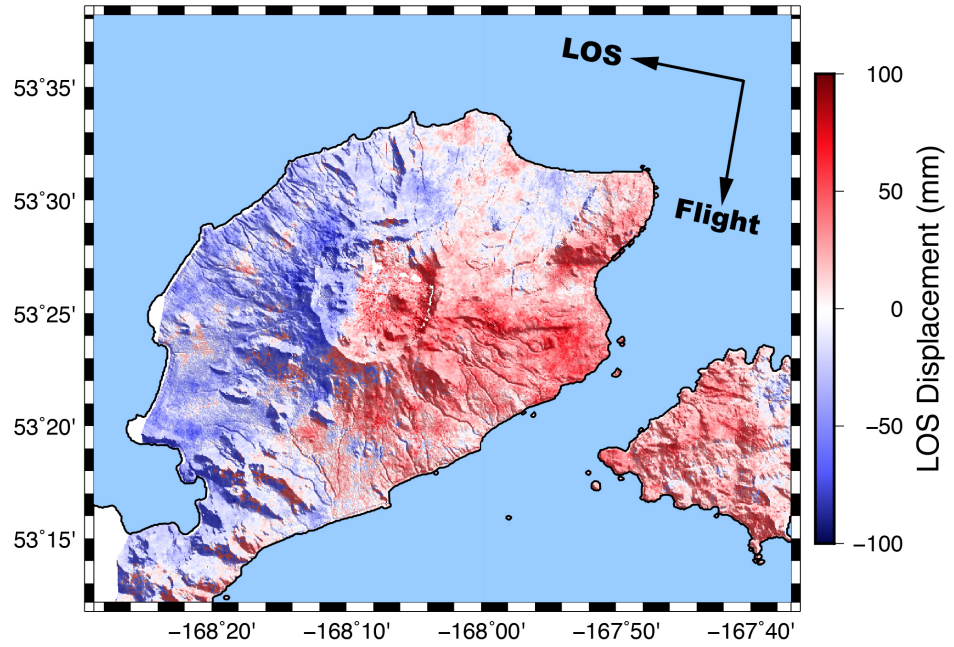

Figure 2.10: SBAS result for descending Sentinel-1, showing cumulative displacement from April 23, 2016 to January 2nd, 2019.

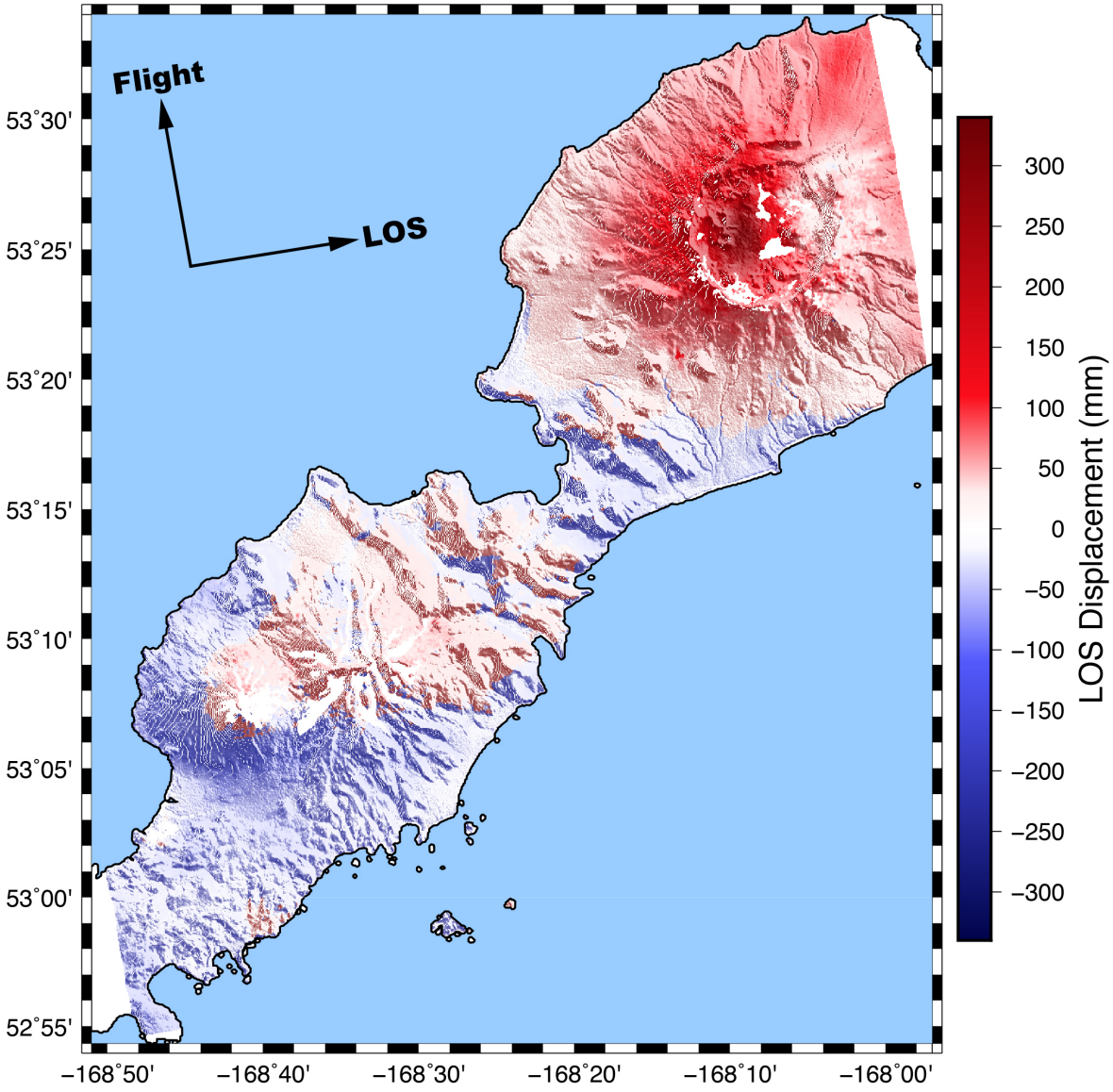

Figure 2.11: SBAS result for ALOS-2, showing cumulative displacement from November 17, 2014 to August 6th, 2018.

2.4 Mogi Model

The data sets previously discussed provide surface deformation patterns that can be used to model the assumedly volcanic source below the surface. The simplest magma chamber model is a Mogi source, which is a point source embedded in a materially homogeneous and mechanically isotropic elastic half-space [Mogi, 1958]. As the source changes in volume due to magma flux, the ground surface is displaced as governed by:

$$\begin{bmatrix} u_x \\ u_y \\ u_z \end{bmatrix} = \frac{(1-\nu)\Delta V}{\pi} \begin{bmatrix} (x-x_0)/R^3 \\ (y-y_0)/R^3 \\ (-z_0)/R^3 \end{bmatrix} \tag{2.1}$$

where u_x, u_y, u_z is the displacement vector at the surface, x_0, y_0, and z_0 define the source location, ν is Poisson's ratio (the ratio of lateral unit strain to longitudinal unit strain), and ΔV is the volume change of the source. The radial distance from the source to the observation point x,y on the surface is given by:

$$R = \sqrt{(x-x_0)^2 + (y-y_0)^2 + (-z_0)^2} \tag{2.2}$$

[Segall, 2010]. Posed as a forward problem, the Mogi model's prediction of the displacement field due to perturbation of the Mogi source can be written as

$$d = Gm \tag{2.3}$$

where d is a vector of displacements, m is a vector of model parameters, and G is the Green's function (Earth response) derived from the Mogi model (Equation 2.1). Since the surface displacements at Okmok are already known from InSAR and GPS, the model parameters can instead be estimated using a least squares inversion. The inversion is done by solving for the

model m^* that minimizes the Euclidean 2-norm:

$$m^* = min(\|d - Gm\|^2) \tag{2.4}$$

This study focuses on recovering the volume change ΔV, so the Green's function matrix G was constructed in the following way. A value of 0.25 was used for ν based on common use arising from laboratory experiments that yield values in the range of 0.15 to 0.3 [Lisowski, 2007]. The source's 3-dimensional location was solved for by performing a grid search over a $50\times50\times50$ grid of x_0,y_0, and z_0 values. The values in the grid correspond to 8 km of depth and 16 km^2 horizontal area. The best fit locations for each data set are those that minimize the root mean square (RMS) error between the modeled and observed surface displacements. Although the volume change was allowed to vary freely through the grid search despite there being a depth/source-strength trade-off, ambiguity in the best-fit depth is reduced due to the high spatial resolution of the data. This is because the well-defined deformation pattern on the surface is governed by upward continuation of the pressure signal: the deeper the source, the broader the deformation pattern. Note that in the grid search results summarized in Figure 2.12, sources deeper than 6 km fit considerably less because they are incapable of producing a deformation signal of short enough wavelength to fit the data, no matter the volume change. Similarly, sources shallower than 2-3 km are incapable of producing deformation patterns of long enough wavelength to fit the data.

After performing the grid search on each of the data sets' cumulative deformation, the best-fit locations were averaged to obtain a depth of 3,560 meters below sea level and a horizontal position of 53.426°N, -168.137°W (see Figure 2.13 for modeled locations and average). This average location was fixed in the Green's function that was used to invert for the volume change over time. The resulting time series is shown in Figure 2.14.

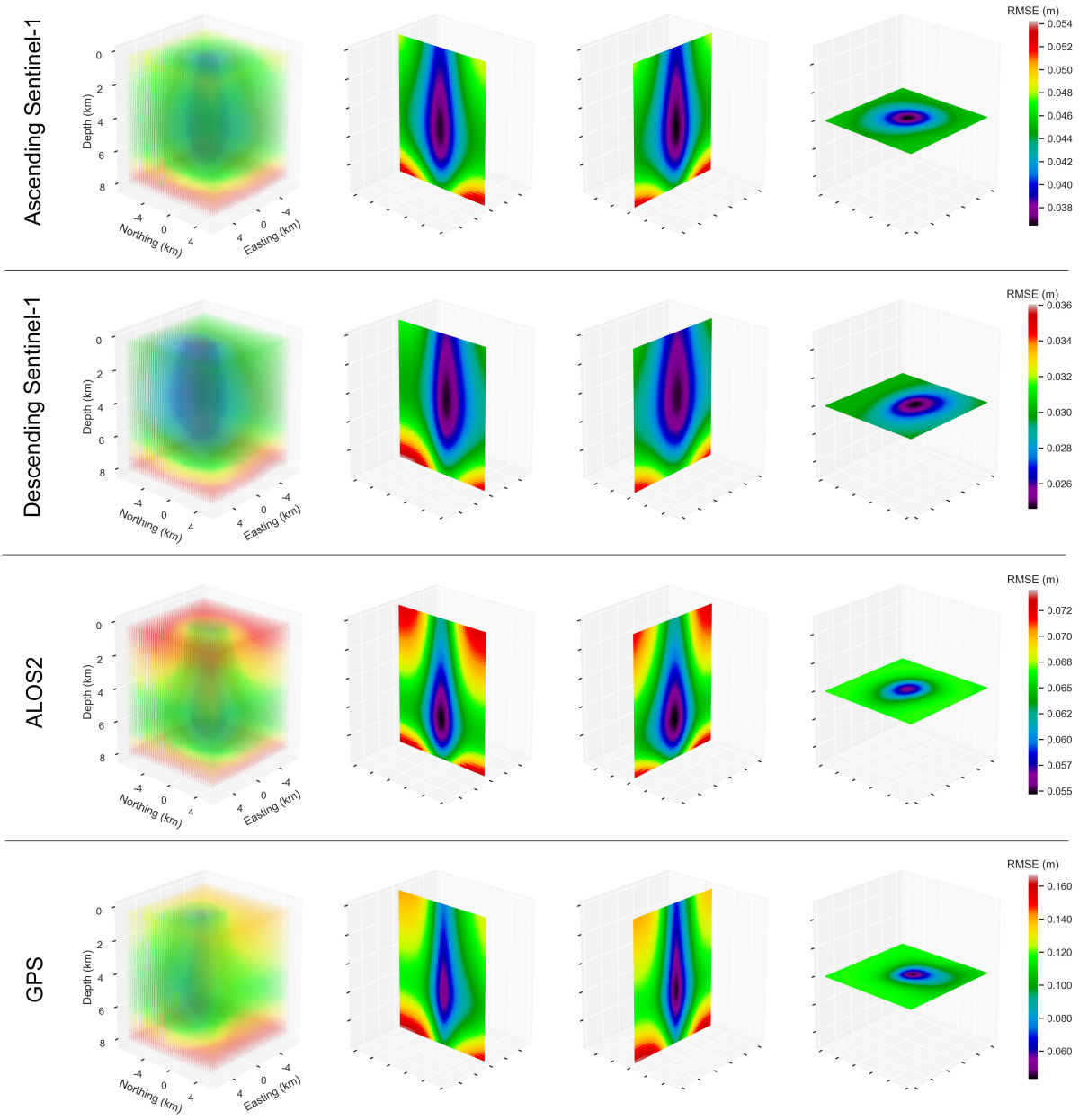

Figure 2.12: Grid search results for each data set. Note the differences in color scale.

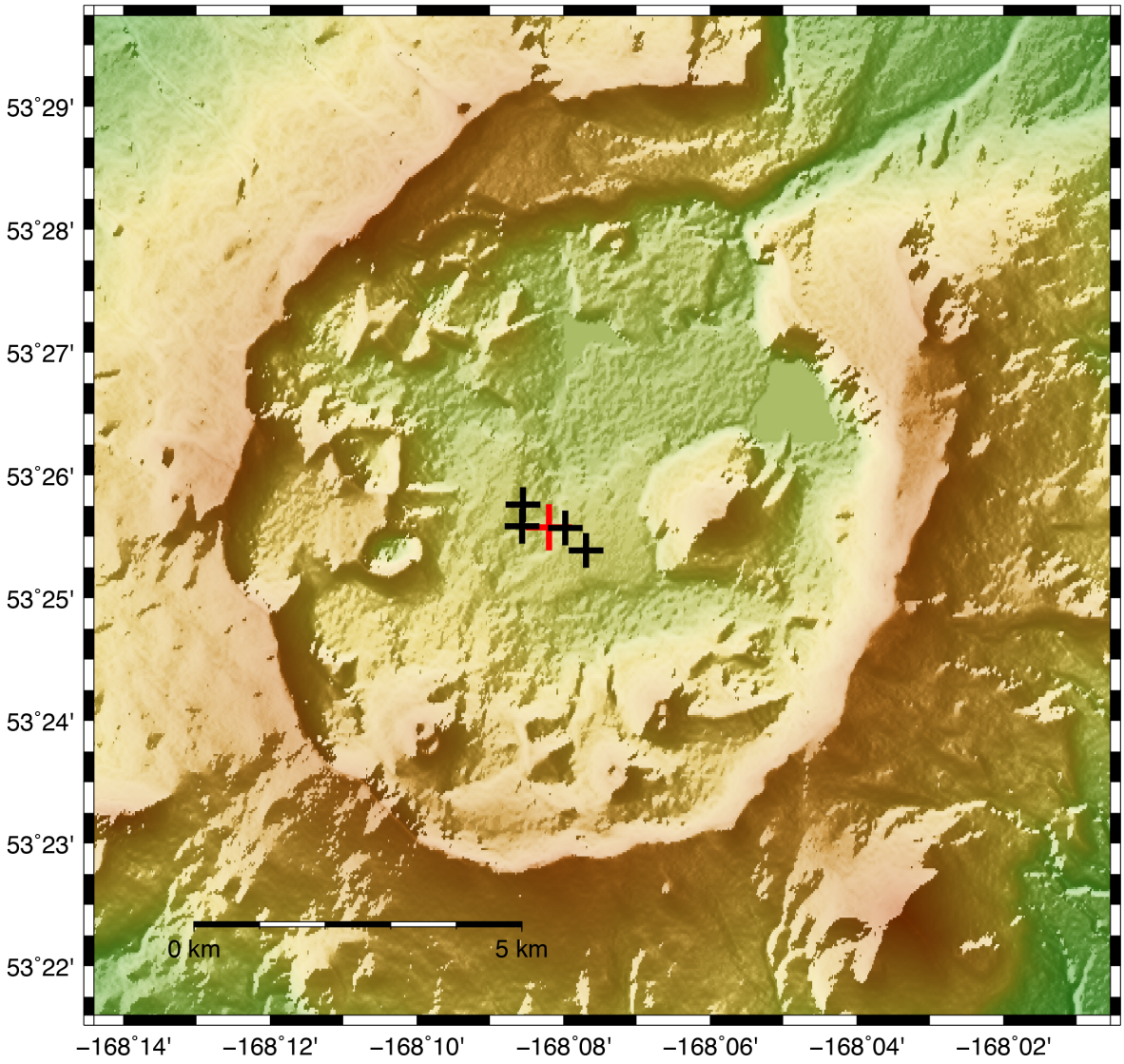

Figure 2.13: Surface projection of the source's modeled horizontal location. The black pluses denote locations obtained by grid search of the 4 data sets while the red plus is the average location.

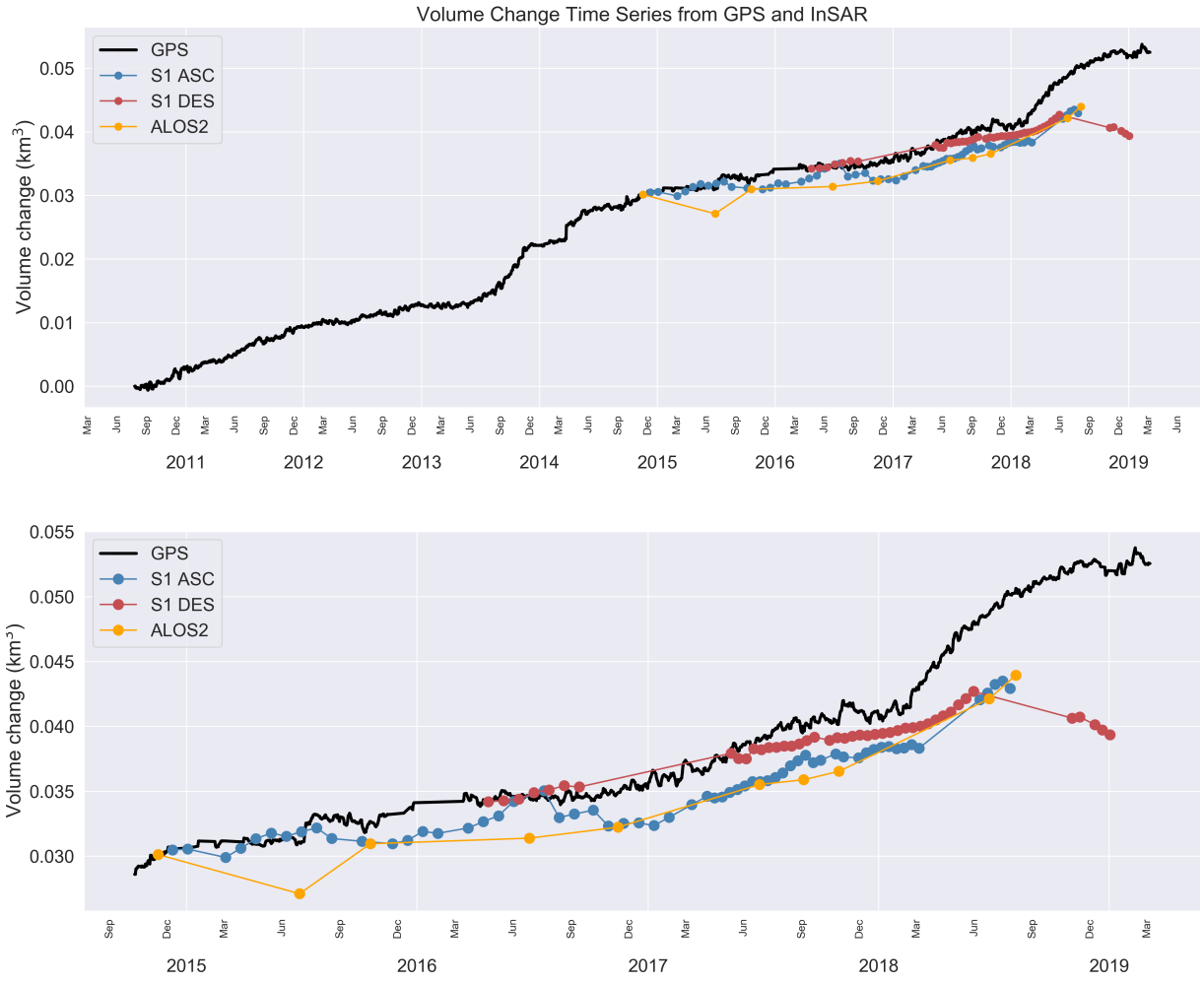

Figure 2.14: Modeled time series of volume change, constructed by performing separate inversions on the InSAR and GPS data sets.

Chapter 3

Discussion

This chapter will explore potential sources of error in the data and the models by first comparing the data sets directly, then evaluating the goodness of fit between the models and the data. The cumulative volume change time series will then be compared to previous studies of Okmok.

3.1 InSAR and GPS Comparison

In order to use solely InSAR in monitoring volcano deformation in cases where GPS is unavailable, potential sources of error must be explored. For regions such as Okmok that do have GPS stations, these errors can be illuminated by comparing data sets under the assumption that the GPS data is free of errors. InSAR only allows for single-component measurements in the radar's line of sight, as opposed to GPS which measures displacement in 3 directions (east, north, and vertical). To check for agreement between the InSAR and GPS data sets, the GPS data must therefore be projected to line of sight by taking the dot product of the displacements with a unit vector given by the satellite's viewing geometry. This unit vector varies between satellites and whether the pass is ascending or descending. Data from the four GPS stations were projected to the three InSAR lines of sight (ascending Sentinel-1, descending Sentinel-1, and ALOS-2) and

compared to the InSAR time series of displacements at those points; the results are summarized in Figures 3.1, 3.2, and 3.3. The InSAR point displacements were spatially averaged over 400 meters centered on the GPS station location to reduce noise caused by decorrelated pixels in the region. Temporal smoothing (median filter of 7 days) has also been applied to the GPS time series.

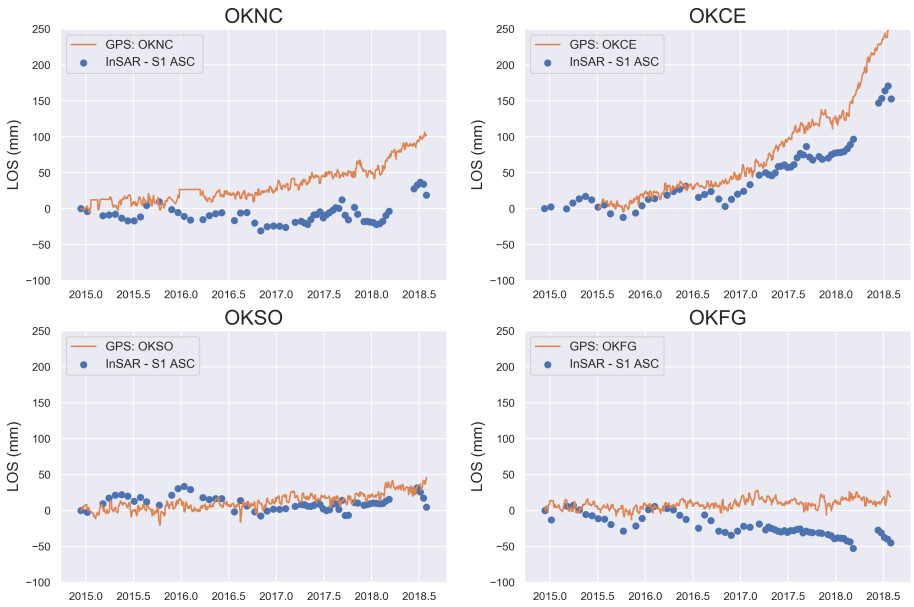

Figure 3.1: Comparison of the ascending Sentinel-1 time series to the GPS time series.

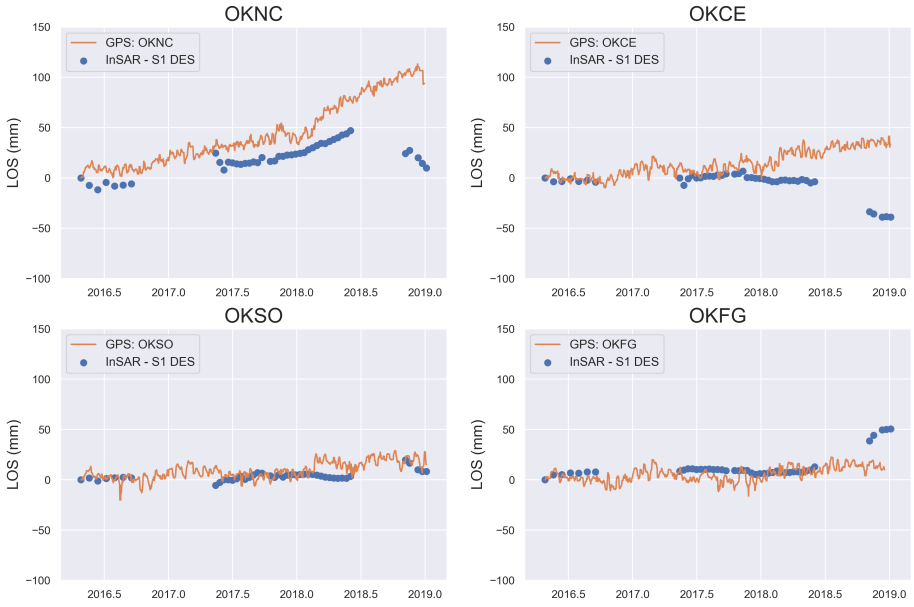

Figure 3.2: Comparison of the descending Sentinel-1 time series to the GPS time series.

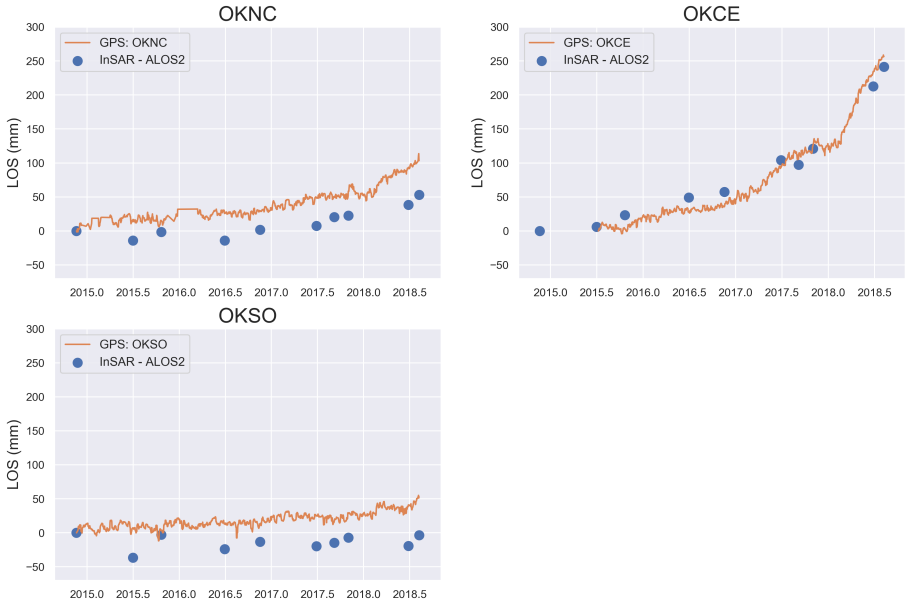

Figure 3.3: Comparison of the ALOS-2 time series to the GPS time series.

The direct comparison between the GPS and InSAR data sets in Figures 3.1, 3.2, and 3.3 reveal some characteristics of the uncertainties in the data. At the stations located inside the range of deformation (OKNC, OKCE, OKSO), most of the InSAR data show less displacement than the GPS data. This could be the result of spatial averaging (400 meters) of the InSAR data that spreads out the deformation signal and reduces its value, removal of the atmospheric signal during the SBAS step, or removal of the linear trend during interferogram processing. The data sets fit better at station OKFG, which could be due to the location's relatively low elevation and consequential lack of snow during even the winter months. OKFG is also located outside of the range of deformation so there is less potential for uncertainties in the InSAR data introduced by unwrapping errors and/or the SBAS time series estimation. This is contradictory, however, to the last five data points of the descending Sentinel-1 data. These five points consistently show poor agreement with the GPS data (even at station OKFG) and are likely the result of the large temporal gap in the InSAR data set. The summer-summer interferograms were added to the time series estimation to bridge gaps such as this one, but there are not yet any summer scenes to connect to those from the summer of 2018, leaving this gap unbridged. SBAS was likely unable to interpolate correctly within the gap because the scenes at the other end are from winter months and therefore unreliable.

Recent studies have used GPS as a means of calibrating InSAR data [Xu et al., 2018, Wei et al., 2010, Tong et al., 2013]. A similar correction was attempted here, but introduced more errors than it solved because Okmok's GPS network is too sparse to create an accurate deformation field model that represents the entire region. This method is therefore better suited to regions with a dense array of GPS receivers, such as Southern California where the method has proven to be effective.

3.2 Model Uncertainties

The use of a Mogi source was chosen based on the computational simplicity of the model and the radially symmetric deformation pattern observed in the InSAR data which suggests a spherical source. Use of a rectangular tensile dislocation source [Okada, 1992] was also attempted, but did not provide reasonable fit to the observed data. Lu and Dzurisin (2010) additionally found that when using a prolate spheroid model on Okmok's deformation preceding the 2008 eruption, the best fit source was nearly spherical and fit the data equally to a Mogi source.

While the source geometry is relatively straightforward for Okmok, the other assumptions made are not as simple. The implementation of the Mogi model in this study assumes that the magma is incompressible, so the source strength is given in terms of volume change instead of pressure change. In reality, magma compressibility can vary greatly depending on the magma's gas content, bubble density, and crystal fraction [Lu and Dzurisin, 2014]. Evaluating the validity of this assumption in depth is outside the scope of this study, but the lavas extruded by Okmok in the past have a mostly basaltic composition which suggests that the magma may have a sufficiently low gas content such that the assumption is reasonable.

Another assumption made by the model is homogeneity of the rock surrounding the source. Accounting for layering or spatial variations with finite element modeling (as was done by Masterlark et al., 2010) would result in a more accurate model, especially in the case of a shield volcano such as Okmok where the near-surface is a layered system of successively erupted material. Okmok's shield structure, however, means that the topographic relief is small enough that the assumed flat surface of the problem domain is acceptable.

The depth/strength ambiguity has no effect on the rate of inflation seen in the time series volume change model because the source depth is fixed through the time series, but it could affect a vertical offset of the absolute value. The goodness of fit of the modeled to the observed InSAR data, however, suggests that the model does not greatly under/overestimate the source

depth. Analysis of the residuals shows that the magnitude of misfit is similar to the magnitude of noise present in the InSAR data when all data sets are taken into consideration (Figures 3.4c,3.5c, and 3.6c. While the ALOS-2 model shows systematic underestimation of the deformation, the descending Sentinel-1 model shows systematic overestimation. This inconsistency is the result of data disagreement and could be improved by implementing a joint inversion that weighs the more reliable data heavier than the rest.

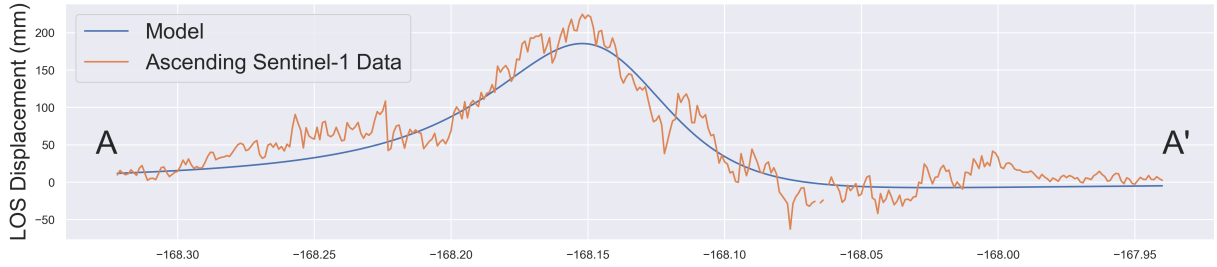

(a) Cross section from A to A' of modeled vs. observed ascending Sentinel-1 displacements.

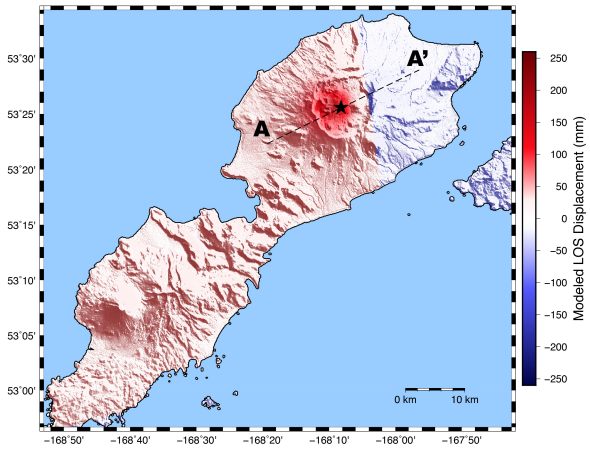

(b) Modeled ascending Sentinel-1 displacements.

(c) Ascending Sentinel-1 residuals (data-model).

Figure 3.4: Plots summarizing the model/data fit of the ascending Sentinel-1 data. These plots only show the model of cumulative volume change, corresponding to the cumulative displacements seen in Figure 2.9.

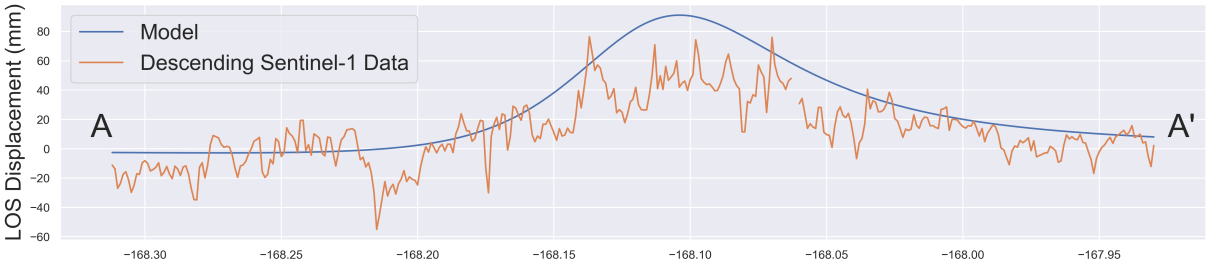

(a) Cross section from A to A' of modeled vs. observed descending Sentinel-1 displacements.

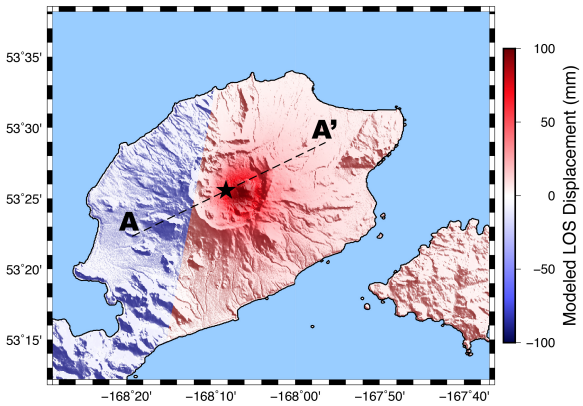

(b) Modeled descending Sentinel-1 displacements.

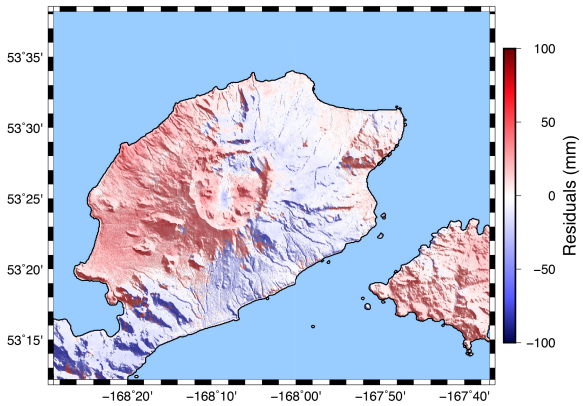

(c) Descending Sentinel-1 residuals (data-model).

Figure 3.5: Plots summarizing the model/data fit of the descending Sentinel-1 data. These plots only show the model of cumulative volume change, corresponding to the cumulative displacements seen in Figure 2.10.

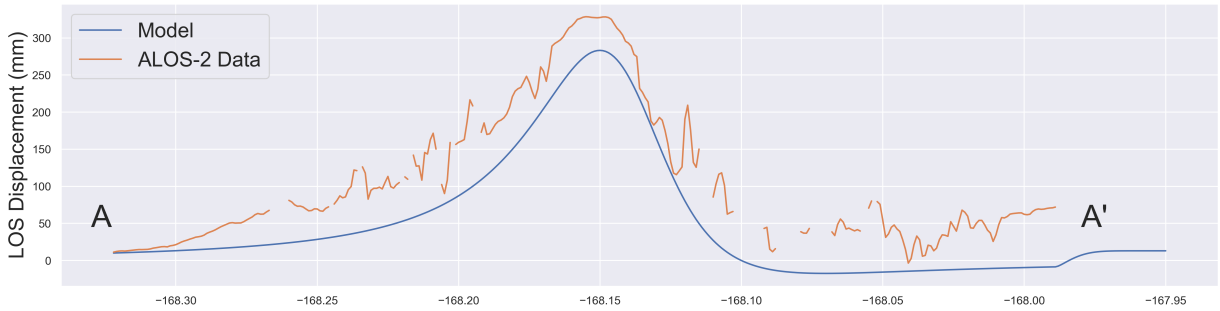

(a) Cross section from A to A' of modeled vs. observed ALOS-2 displacements.

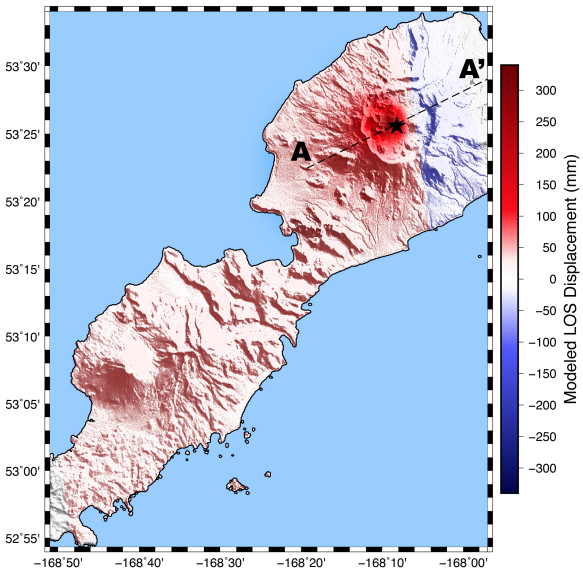

(b) Modeled ALOS-2 displacements.

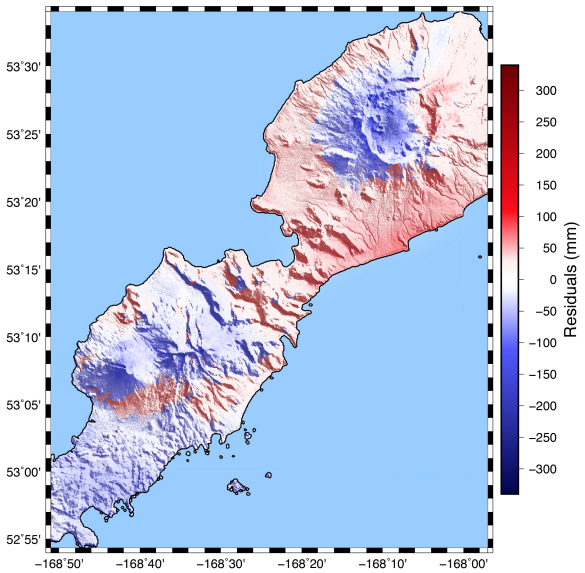

(c) ALOS-2 residuals (data-model).

Figure 3.6: Plots summarizing the model/data fit of the ALOS-2 data. These plots only show the model of cumulative volume change, corresponding to the cumulative displacements seen in Figure 2.11.

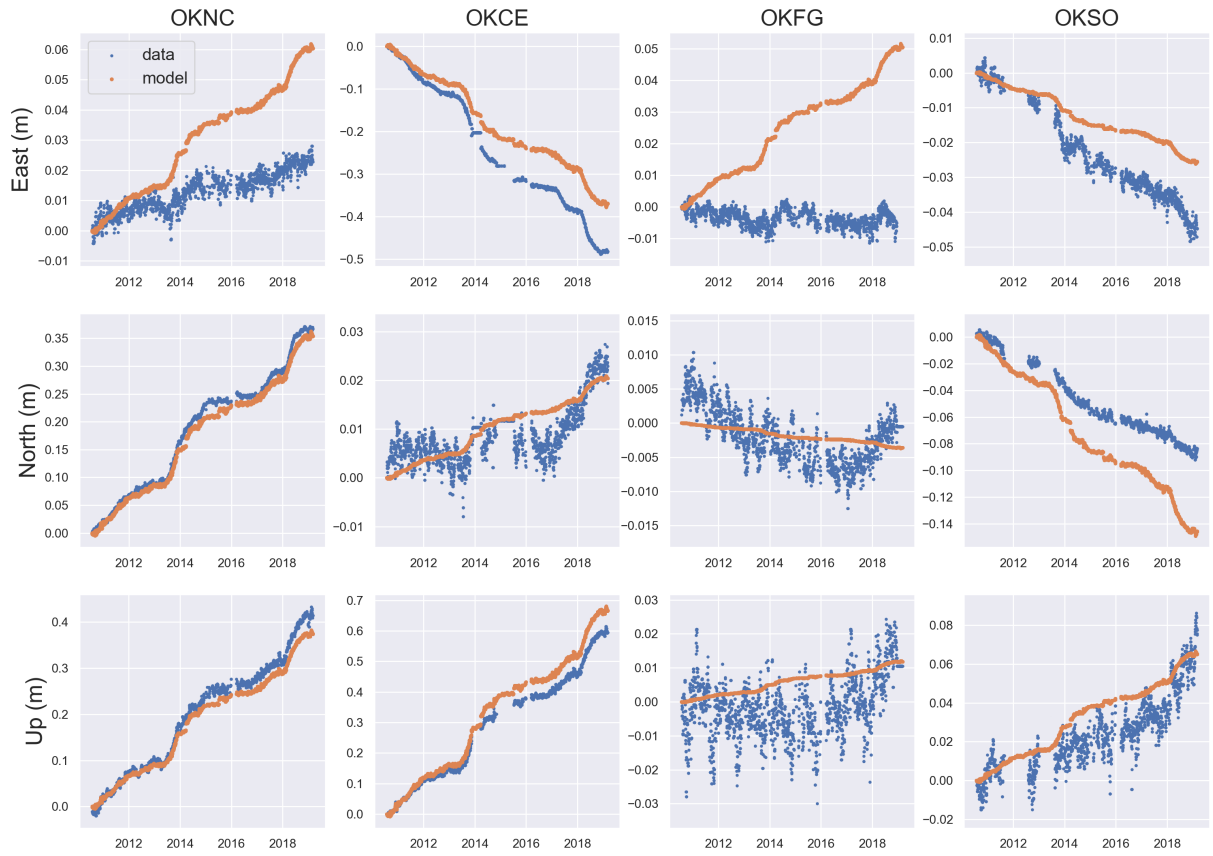

Figure 3.7: Comparison between the modeled (yellow dots) and observed (blue dots) displacements for the East, North, and up components at each GPS station location.

3.3 Comparison to Previous Studies

Extending the time series to before or just after the 2008 eruption makes the volume change value more meaningful and allows for a more significant comparison to previous pre-eruptive inflation episodes. The time period from 2008 to 2014 was considered by Qu et al., 2015 using InSAR data via the Envisat and TerraSAR-X satellites. The cumulative volume change value obtained by Qu et al., 2015 is approximately equal to the value obtained in this study between late 2014 and early 2019, suggesting that recharge has increased in rate. While our study does not consider InSAR data prior to 2015, the GPS data we use overlaps with the Qu et al., 2015

data set between late 2010 and late 2014. The volume change time series from both studies agree during this overlapping period. The source depth found by Qu et al., 2015 of 3.9 $\pm$ 0.3 km is also in agreement with the source depth of 3.56 km found in this study. It is therefore reasonable to assume that the modeling results can be connected in an extended time series, which is shown in Figure 3.8. Figure 3.8 also shows this time series extended to include other studies that have used GPS and InSAR to model volume change over time.

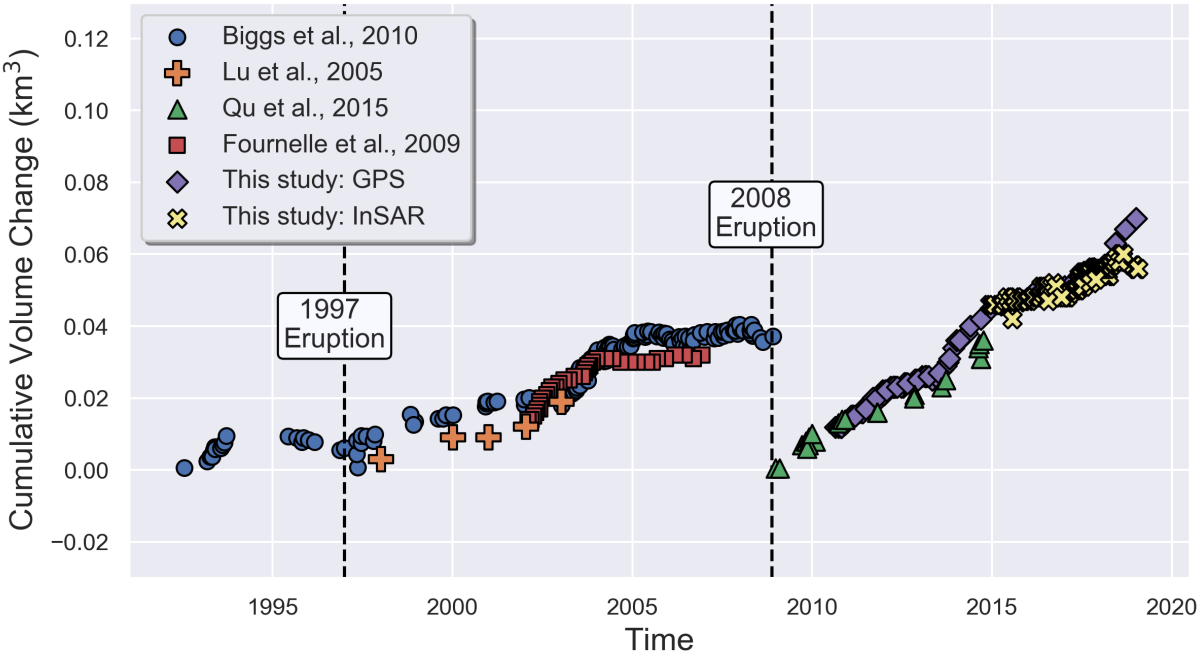

Figure 3.8: Cumulative volume change time series, modified from Biggs et al., 2010, Lu et al., 2005, Qu et al., 2015, and Fournelle et al., 2009.

While inflation is continuous between the 1997 and 2008 eruptions, it is not steady, indicating that magma supply varies with time. The inflation prior to the 2008 eruption suggests that Okmok's potential recharge regime is governed by rapid inflation immediately following an eruption, then a declined rate of inflation as the next eruption gets closer. Although the absolute volume change prior to the 1997 eruption is unknown since data coverage only began in 1992, the plateauing behavior preceding the eruption is still observed and is similar in du-

ration to that preceding the 2008 eruption. This pattern has been observed at other volcanoes [Dvorak and Dzurisin, 1997] and has been suggested to be indicative of the reservoir reaching a critical state of pressurization in which the surrounding rock can halt the supply of magma from depth [Lu and Dzurisin, 2014]. If this is the case, then the volume change time series presented in this thesis shows that Okmok's magma reservoir has already reached the proposed critical amount (based on that reached by previous pre-eruptive inflation events), yet it still continues to inflate. This suggests that though Okmok has exhibited the pattern twice consistently in the past, the interpretation of it representing a critical state of pressurization might not be the reason for the inflation rate decline preceding eruptions. Lu and Dzurisin (2014) also state that volcanoes exhibiting a steadily increasing inflation rate prior to eruptions are more commonly observed, and that there is likely a spectrum between the two cases. The results presented in this thesis are more supportive of Okmok being capable of both, when combined with previous studies. Interpreting declined rate of inflation at Okmok as an indicator for high eruptive potential must therefore be used with caution.

Chapter 4

Conclusions

Three InSAR data sets (ascending Sentinel-1, descending Sentinel-1, ALOS-2) and data from four continuous GPS stations reveal that Okmok's ground surface has been inflating since the 2008 eruption. The shape and magnitude of the deformation pattern are consistent with Okmok's previous inflation episodes observed by other SAR systems. The result of modeling Okmok's magma chamber with a Mogi source located at 3.56 km depth provides a volume change time series that suggests Okmok's magma chamber has exceeded the level of recharge reached before previous eruptions in 1997 and 2008.

Sentinel-1 is a young satellite system and has not yet been used in a published study of Okmok Volcano. Using both ascending and descending passes has shown that Sentinel-1's C-band wavelength is usable for constructing a time series when there is high temporal resolution (seen in the ascending data), but fails when there are large data gaps (seen in the descending data). Alternatively, ALOS-2's longer L-band wavelength provides good correlation in interferograms that span as long as three years, so temporal resolution is not as crucial. For InSAR to be reliable in constructing a deformation time series in regions of great seasonal variability such as the Aleutians, the optimal combination is high temporal resolution and longer radar wavelength.

Future work on this project includes performing a joint inversion of the interferograms

themselves, instead of comparing separate inversions of the data sets' SBAS results. Though the SBAS time series estimation would be circumvented by using this method, the atmospheric phase correction included in the SBAS step could still be calculated and subtracted from the interferograms prior to the inversion. Additionally, the source's horizontal location and depth could be allowed to vary through the time series by turning the problem into a non-linear inversion and simultaneously solving for location and volume change, instead of a grid search for location and a linear inversion of volume change. Doing so would provide a more thorough way of calculating confidence intervals on all of the estimated parameters.

Okmok's past two pre-eruptive inflations have been used to suggest that a reduced rate of inflation is indicative of increased eruptive likelihood due to the magma chamber reaching a critical state of pressurization. The results shown in this thesis suggest that Okmok has already reached this critical state, but has not yet shown any sign of decreased rate of inflation. Due to this inconsistency, relying on Okmok's inflation rate as a means of placing constraints on its eruptive potential must be done with caution.

Appendix A

Persistent Scatterers

As discussed in Section 1.3.2, loss of coherence occurs as a result of changes in the scattering characteristics of a resolution cell. If portions of a scene are covered in snow, vegetation, or moist soil, but these portions include isolated scatterers that remain coherent over time (such as large boulders, buildings, or roads), these scatterers can be weighed more heavily than the surrounding decorrelated region during processing to improve correlation in these areas. This was attempted for the 61 ascending Sentinel-1 scenes by first following the method of Ferretti et al., 2001, in which persistent scatterers are identified by computing each pixel's amplitude dispersion:

$$D_A = \frac{\sigma_A}{\mu_A} \tag{A.1}$$

where σ_A is the standard deviation of the mean amplitude of the image and μ_A is the mean amplitude of the entire stack. The remaining steps follow the method of Lyons and Sandwell (2003), who instead used the inverse square of the amplitude dispersion to make a weighing factor:

$$s^2 = (\frac{\mu_A}{\sigma_A})^2 \tag{A.2}$$

Highly dispersive areas, such as snowy or vegetated regions, have a low phase stability and therefore a low weighing factor. This weighing factor was then multiplied by the real and imaginary components of each pixel just before the step in which the interferogram is convolved with a gaussian filter. Giving reliable pixels (high s^2) extra confidence increases the amplitude of areas with high phase stability while leaving the phase of the pixel alone. After filtering, the remaining steps of processing the interferogram remain the same.

As is shown in Figure A.1, the scattering weights across the scene are all too small to be beneficial. Note that the ”best” regions are those on the very edges of the island, where there are rocky cliffs and beach sand with little vegetation and no snow cover. Improving correlation in these areas is not helpful since they are outside the range of observed deformation.

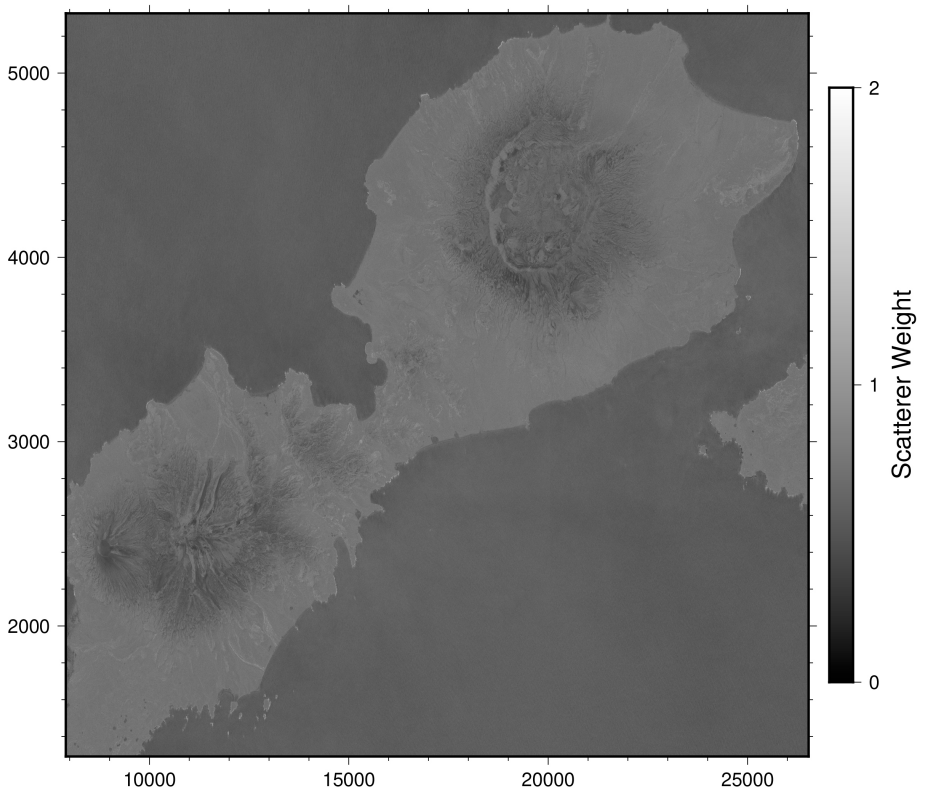

Figure A.1: Map in radar coordinates of the scattering weight s^2 of each pixel.

An example of an interferogram that has been processed with and without this method is shown in Figure A.2. The rest of the interferograms from the ascending Sentinel-1 stack show similar results. The method likely had little effect because there are no isolated dependable regions within the decorrelated regions, especially when the area becomes completely snow-covered in the winter. The method (as applied to this data set) could potentially be improved by instead computing the scattering weights from a stack of only winter scenes, instead of the entire stack. This would allow for more variance in the weights by not allowing them to become biased by the summer scenes that have good overall correlation.

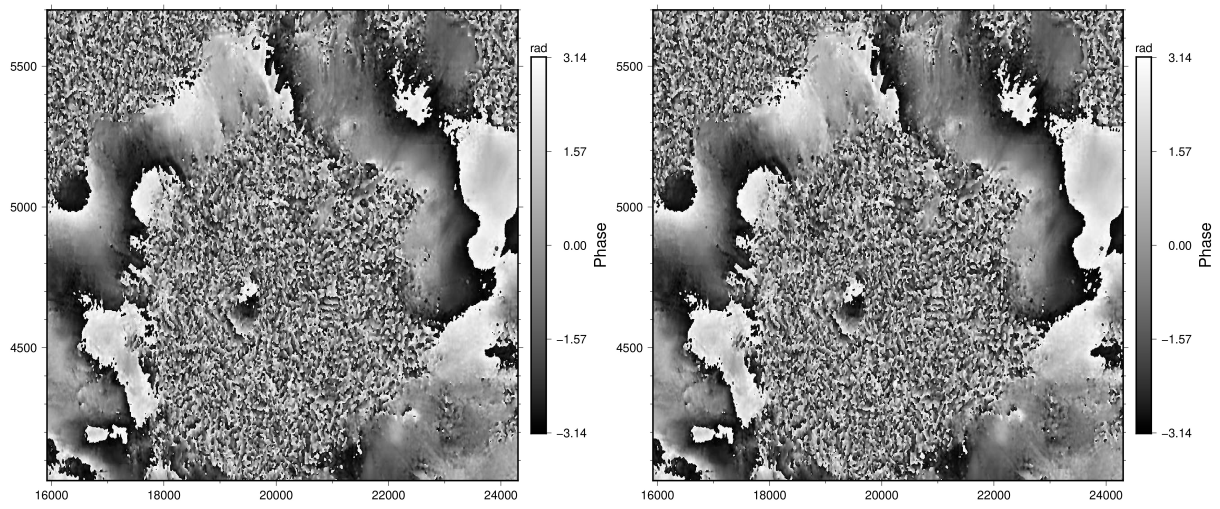

(a) Without PS

(b) With PS

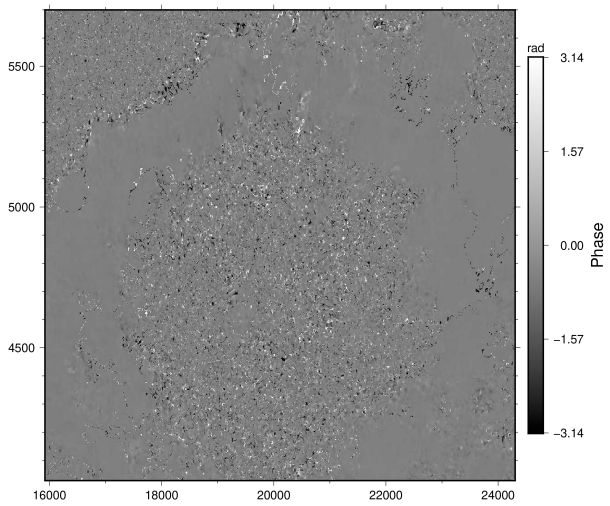

(c) Difference (without PS - with PS)

Figure A.2: Persistent scatterers result for an ascending Sentinel-1 interferogram spanning January 5, 2018 - June 10, 2019. The region shown is centered on the caldera. Image is in radar coordinates.

Bibliography

[Ben-Avraham and Cooper, 1981] Ben-Avraham, Z. and Cooper, A. K. (1981). Early evolution of the Bering Sea by collision of oceanic rises and North Pacific subduction zones. *GSA Bulletin*, 92(7):485–495.

[Berardino et al., 2002] Berardino, P., Fornaro, G., Lanari, R., Member, S., and Sansosti, E. (2002). A New Algorithm for Surface Deformation Monitoring Based on Small Baseline Differential SAR Interferograms. *IEEE Transactions on Geoscience and Remote Sensing*, 40(11):2375–2383.

[Biggs et al., 2014] Biggs, J., Ebmeier, S. K., Aspinall, W. P., Lu, Z., Pritchard, M. E., Sparks, R. S. J., and Mather, T. A. (2014). Global link between deformation and volcanic eruption quantified by satellite imagery. *Nature Communications*, 5(1):3471.

[Biggs et al., 2010] Biggs, J., Lu, Z., Fournier, T., and Freymueller, J. T. (2010). Magma flux at Okmok Volcano, Alaska, from a joint inversion of continuous GPS, campaign GPS, and interferometric synthetic aperture radar. *Journal of Geophysical Research*, 115(B12):B12401.

[Blewitt, 2018] Blewitt, G. (2018). Harnessing the GPS Data Explosion for Interdisciplinary Science. *Eos*, 99.

[Brophy and Marsh, 1986] Brophy, J. G. and Marsh, B. D. (1986). On the Origin of High-Alumina Arc Basalt and the Mechanics of Melt Extraction. *Journal of Petrology*, 27(4):763–789.

[Chen and Zebker, 2000] Chen, C. W. and Zebker, H. A. (2000). Network approaches to two-dimensional phase unwrapping: intractability and two new algorithms. *Journal of the Optical Society of America A*, 17(3):401.

[Davis, 1986] Davis, P. M. (1986). Surface deformation due to inflation of an arbitrarily oriented triaxial ellipsoidal cavity in an elastic half-space, with reference to Kilauea volcano, Hawaii. *Journal of Geophysical Research: Solid Earth*, 91(B7):7429–7438.

[Dvorak and Dzurisin, 1997] Dvorak, J. J. and Dzurisin, D. (1997). Volcano geodesy: The search for magma reservoirs and the formation of eruptive vents. *Reviews of Geophysics*, 35(3):343–384.

[Fernández et al., 2017] Fernández, J., Pepe, A., Poland, M. P., and Sigmundsson, F. (2017). Volcano Geodesy: Recent developments and future challenges. *Journal of Volcanology and Geothermal Research*, 344:1–12.

[Ferretti et al., 2001] Ferretti, A., Prati, C., and Rocca, F. (2001). Permanent scatterers in SAR interferometry. *IEEE Transactions on Geoscience and Remote Sensing*, 39(1):8–20.

[Fialko et al., 2001] Fialko, Y., Simons, M., and Agnew, D. (2001). The complete (3-D) surface displacement field in the epicentral area of the 1999 M 7.1 Hector Mine Earthquake, California, from space geodetic observations. *Geophysical Research Letters*, 28(16):3063–3066.

[Finney et al., 2008] Finney, B., Turner, S., Hawkesworth, C., Larsen, J., Nye, C., George, R., Bindeman, I., and Eichelberger, J. (2008). Magmatic Differentiation at an Island-arc Caldera: Okmok Volcano, Aleutian Islands, Alaska. *Journal of Petrology*, 49(5):857–884.

[Fournelle et al., 1994] Fournelle, J. H., Marsh, B. D., and Myers, J. D. (1994). Age, character, and significance of Aleutian arc volcanism. In *The Geology of Alaska*, volume G-1, chapter 23, pages 723–757. The Geological Society of America.

[Fournier et al., 2009] Fournier, T., Freymueller, J., and Cervelli, P. (2009). Tracking magma volume recovery at okmok volcano using GPS and an unscented kalman filter. *Journal of Geophysical Research: Solid Earth*, 114(2):1–18.

[Freymueller and Kaufman, 2010] Freymueller, J. T. and Kaufman, A. M. (2010). Changes in the magma system during the 2008 eruption of Okmok volcano, Alaska, based on GPS measurements. *Journal of Geophysical Research*, 115(B12):B12415.

[Kay, 1980] Kay, R. W. (1980). Volcanic Arc Magmas: Implications of a Melting-Mixing Model for Element Recycling in the Crust-Upper Mantle System. *The Journal of Geology*, 88(5):497–522.

[Kay and Kay, 1994] Kay, S. M. and Kay, R. W. (1994). Aleutian magmas in space and time. In *The Geology of Alaska*, volume G-1, pages 687–717. The Geological Society of America.

[Larsen et al., 2009] Larsen, J., Neal, C., Webley, P., Freymueller, J., Haney, M., McNutt, S., Schneider, D., Prejean, S., Schaefer, J., and Wessels, R. (2009). Eruption of Alaska Volcano Breaks Historic Pattern. *Eos, Transactions American Geophysical Union*, 90(20):173.

[Larsen et al., 2013] Larsen, J. F., Śliwiński, M. G., Nye, C., Cameron, C., and Schaefer, J. R. (2013). The 2008 eruption of Okmok Volcano, Alaska: Petrological and geochemical constraints on the subsurface magma plumbing system. *Journal of Volcanology and Geothermal Research*, 264:85–106.

[Lathram, 1974] Lathram, E. H. (1974). Aleutian Arc. *Geological Society, London, Special Publications*, 4(1):553–561.

[Lisowski, 2007] Lisowski, M. (2007). Analytical volcano deformation source models. In *Volcano Deformation*, pages 279–304. Springer Berlin Heidelberg, Berlin, Heidelberg.

[Lu and Dzurisin, 2010] Lu, Z. and Dzurisin, D. (2010). Ground surface deformation patterns, magma supply, and magma storage at Okmok volcano, Alaska, from InSAR analysis: 2. Coeruptive deflation, July-August 2008. *Journal of Geophysical Research*, 115(B5):B00B03.

[Lu and Dzurisin, 2014] Lu, Z. and Dzurisin, D. (2014). *InSAR Imaging of Aleutian Volcanoes: Monitoring a Volcanic Arc from Space*, page 390. Praxis Publishing.

[Lu et al., 2010] Lu, Z., Dzurisin, D., Biggs, J., Wicks, C., and McNutt, S. (2010). Ground surface deformation patterns, magma supply, and magma storage at Okmok volcano, Alaska, from InSAR analysis: 1. Intereruption deformation, 1997-2008. *Journal of Geophysical Research*, 115(B5):B00B02.

[Lu et al., 2003] Lu, Z., Fielding, E., Patrick, M., and Trautwein, C. (2003). Estimating lava volume by precision combination of multiple baseline spaceborne and airborne interferometric synthetic aperture radar: the 1997 eruption of Okmok Volcano, Alaska. *IEEE Transactions on Geoscience and Remote Sensing*, 41(6):1428–1436.

[Lu et al., 2005] Lu, Z., Masterlark, T., and Dzurisin, D. (2005). Interferometric synthetic aperture radar study of Okmok volcano, Alaska, 1992-2003: Magma supply dynamics and postemplacement lava flow deformation. *Journal of Geophysical Research: Solid Earth*, 110(B2):B02403–B02403.

[Lyons and Sandwell, 2003] Lyons, S. and Sandwell, D. (2003). Fault creep along the southern San Andreas from interferometric synthetic aperture radar, permanent scatterers, and stacking. *Journal of Geophysical Research: Solid Earth*, 108(B1):11–1–11–24.

[Mann et al., 2002] Mann, D., Freymueller, J., and Lu, Z. (2002). Deformation associated with the 1997 eruption of Okmok volcano, Alaska. *Journal of Geophysical Research: Solid Earth*, 107(B4):ETG 7–1–ETG 7–12.

[Marsh, 1976] Marsh, B. D. (1976). Some Aleutian Andesites: Their Nature and Source. *The Journal of Geology*, 84(1):27–45.

[Masterlark et al., 2010] Masterlark, T., Haney, M., Dickinson, H., Fournier, T., and Searcy, C. (2010). Rheologic and structural controls on the deformation of Okmok volcano, Alaska: FEMs, InSAR, and ambient noise tomography. *Journal of Geophysical Research: Solid Earth*, 115:1–22.

[McTigue, 1987] McTigue, D. F. M. (1987). Elastic Stress and Deformation Near a Finite Spherical Magma Body: Resolution of the Point Source Paradox. *Journal of Geophysical Research*, 92(B12):931–943.

[Miller et al., 1998] Miller, T., McGimsey, R., Richter, D., Riehle, J., Nye, C., Yount, M., and Dumoulin, J. A. (1998). Catalog of the historically active volcanoes of Alaska. Technical report, U.S. Geological Survey.

[Miyagi et al., 2004] Miyagi, Y., Freymueller, J. T., Kimata, F., Sato, T., and Mann, D. (2004). Surface deformation caused by shallow magmatic activity at Okmok volcano, Alaska, detected by GPS campaigns 2000-2002. *Earth, Planets and Space*, 56(10):29–32.

[Mogi, 1958] Mogi, K. (1958). Relations between the eruptions of various volcanoes and the deformations of the ground surfaces around them. *Bull. Earthq. Res. Inst.*, 36:99–134.

[Morris and Hart, 1986] Morris, J. and Hart, S. (1986). Isotopic and incompatible element constraints on the genesis of island arc volcanics from Cold Bay and Amak Island, Aleutians, and implications for mantle structure: Reply to a Critical Comment by M. R. Perfit and R. W. Kay. *Geochimica et Cosmochimica Acta*, 50(3):483–487.

[Ohlendorf et al., 2014] Ohlendorf, S. J., Thurber, C. H., Pesicek, J. D., and Prejean, S. G. (2014). Seismicity and seismic structure at Okmok Volcano, Alaska. *Journal of Volcanology and Geothermal Research*, 278-279:103–119.

[Okada, 1992] Okada, Y. (1992). Internal deformation due to shear and tensile faults in a half-space. *Bulletin of the Seismological Society of America*, 82(2):1018–1040.

[Patrick et al., 2003] Patrick, M., Dehn, J., Papp, K., Lu, Z., Dean, K., Moxey, L., Izbekov, P., and Guritz, R. (2003). The 1997 eruption of Okmok Volcano, Alaska: a synthesis of remotely sensed imagery. *Journal of Volcanology and Geothermal Research*, 127(1-2):87–105.

[Qu et al., 2015] Qu, F., Lu, Z., Poland, M., Freymueller, J., Zhang, Q., and Jung, H.-S. (2015). Post-Eruptive Inflation of Okmok Volcano, Alaska, from InSAR, 20082014. *Remote Sensing*, 7(12):16778–16794.

[Rees, 2012] Rees, W. G. (2012). *Physical Principles of Remote Sensing*, pages 307–312. Cambridge University Press, Cambridge.

[Rosen et al., 1996] Rosen, P. A., Hensley, S., Zebker, H. A., Webb, F. H., and Fielding, E. J. (1996). Surface deformation and coherence measurements of Kilauea Volcano, Hawaii, from SIR-C radar interferometry. *Journal of Geophysical Research: Planets*, 101(E10):23109–23125.

[Sandwell et al., 2011] Sandwell, D., Mellors, R., Tong, X., Wei, M., and Wessel, P. (2011). GMTSAR: An InSAR Processing System Based on Generic Mapping Tools. Technical report, Lawrence Livermore National Laboratory.

[Segall, 2010] Segall, P. (2010). *Earthquake and volcano deformation*, pages 207–212. Princeton University Press.

[Segall and Davis, 1997] Segall, P. and Davis, J. L. (1997). GPS Applications for Geodynamics and Earthquake Studies. *Annual Review of Earth and Planetary Sciences*, 25(1):301–336.

[Steketee, 1958] Steketee, J. A. (1958). On Volterra's dislocations in a semi-infinite elastic medium. *Canadian Journal of Physics*, 36(2):192–205.

[Tong et al., 2013] Tong, X., Sandwell, D. T., and Smith-Konter, B. (2013). High-resolution interseismic velocity data along the San Andreas Fault from GPS and InSAR. *Journal of Geophysical Research: Solid Earth*, 118(1):369–389.

[Tymofyeyeva and Fialko, 2015] Tymofyeyeva, E. and Fialko, Y. (2015). Mitigation of atmospheric phase delays in InSAR data, with application to the eastern California shear zone. *Journal of Geophysical Research: Solid Earth*, 120(8):5952–5963.

[Wei et al., 2010] Wei, M., Sandwell, D., and Smith-Konter, B. (2010). Optimal combination of InSAR and GPS for measuring interseismic crustal deformation. *Advances in Space Research*, 46(2):236–249.

[Xu et al., 2018] Xu, X., Ward, L. A., Jiang, J., SmithKonter, B., Tymofyeyeva, E., Lindsey, E. O., Sylvester, A. G., and Sandwell, D. T. (2018). Surface Creep Rate of the Southern San Andreas Fault Modulated by Stress Perturbations From Nearby Large Events. *Geophysical Research Letters*, 45(19):10,259–10,268.

[Yang and Davis, 1986] Yang, X.-M. and Davis, P. M. (1986). Deformation due to a rectangular tension crack in an elastic half-space. *Bulletin of the Seismological Society of America*, 76(3):865–881.